EES Catalysis

REVIEW ARTICLE

View Article Online
View Journal | View Issue

Cite this: *EES Catal.*, 2023, **1**, 230

Recent advances in perovskite oxide electrocatalysts for Li–O_2 batteries

Lulu Lyu,†[a] Seonyong Cho†[a] and Yong-Mook Kang *[abc]

Received 7th February 2023,
Accepted 16th March 2023

DOI: 10.1039/d3ey00028a

rsc.li/eescatalysis

Lithium–oxygen batteries (LOBs) have been anticipated as promising energy-storage devices; however, their practical application is plagued by low energy efficiency, small capacity, and the short cycle life. When applied as air cathodes for LOBs, perovskite oxides exhibit an enormous potential for favorable battery performance due to their catalytic activity for the oxygen reduction reaction (ORR) and oxygen evolution reaction (OER). Their tunable compositions, diverse structures and unique electronic properties allow flexible manipulation of their catalytic activity. This mini-review comprehensively describes recent advances in perovskite oxide electrocatalysts for LOBs. First, the energy-storage mechanism of LOBs and crucial catalytic descriptors of perovskites for the ORR/OER are analyzed. Then, several ingenious tactics to promote the catalytic activity of perovskite oxides are highlighted. A discussion of synthetic protocols for the preparation of perovskite oxides follows, including how the nanostructure, morphology and composition of perovskite oxides can be controlled by different methods and the effect of these on catalytic performance. Additionally, A-/B-/O-site regulation, oxygen vacancies, and the composites of perovskites and functional materials are thoroughly investigated. Finally, we summarize the challenges and outlook of perovskite oxide electrocatalysts for LOBs.

Broader context

The transition from fossil fuels to renewable energy is a pivotal approach to realizing a low-carbon economy, which stimulates the exploration of electrochemical energy storage devices. Lithium–oxygen batteries (LOBs) have been regarded as promising energy-storage systems, while their inferior energy efficiency, low capacity, and poor cycle life greatly hinder their practical applications. Owing to their catalytic activity for the oxygen reduction reaction (ORR) and oxygen evolution reaction (OER), perovskite oxides with a formula of ABO_3 have been investigated as air cathodes for LOBs. Their catalytic activity can be flexibly adjusted by different cation/anion species, distinct nanostructures and unique electronic properties. This mini-review aims to comprehensively provide recent advances in perovskite oxide electrocatalysts for LOBs. It begins with introducing the fundamental energy-storage mechanism of LOBs, and catalytic descriptors of perovskites for the ORR/OER. Next, strategies to improve the catalytic activity of perovskite oxides are highlighted, including the size effect, nanostructure engineering, A-/B-/O-site regulation, oxygen vacancies, and composites of perovskites with other functional materials. Finally, the challenges and outlook of perovskite oxide electrocatalysts for LOBs are given.

1. Introduction

World energy consumption is expected to be 50% higher than 2018 levels (576 EJ) by 2050 (864 EJ). To achieve net zero fossil fuel use by 2050, the annual growth rate of renewable energy production must expand by a factor of 6–8.[1] The soaring demand for electrical energy storage and conversion systems has driven exploration into metal–ion batteries, metal–air batteries, and redox–flow batteries.[2–6] Lithium–air batteries have a superior theoretical energy density of above 5000 W h kg^{-1} (Fig. 1), and a large theoretical open circuit voltage of 2.96 V (eqn (1)).[6–8] Electric vehicles using these batteries may have a driving range of more than 550 kilometers.[9] As shown in Fig. 2(a), lithium–oxygen batteries (LOBs) are composed of a metallic lithium anode, an air cathode and a Li^+-containing aprotic electrolyte.[10–14] The oxygen reduction reaction (ORR) and oxygen evolution reaction (OER) occurring at the cathode dominate the discharging and charging processes of LOBs, respectively.[15–19]

$$2Li^+ + 2e^- + O_2 \underset{\text{Charge}}{\overset{\text{Discharge}}{\rightleftharpoons}} Li_2O_2 (E_0 = 2.96\ \text{V}\ \textit{vs.}\ Li/Li^+) \quad (1)$$

[a] *Department of Materials Science and Engineering, Korea University, Seoul 02841, Republic of Korea. E-mail: dake1234@korea.ac.kr*
[b] *KU-KIST Graduate School of Converging Science and Technology, Korea University, Seoul, 02841, Republic of Korea*
[c] *Energy Storage Research Center, Clean Energy Research Division, Korea Institute of Science and Technology (KIST), Seoul 02792, Republic of Korea*
† These authors contributed equally to this work.

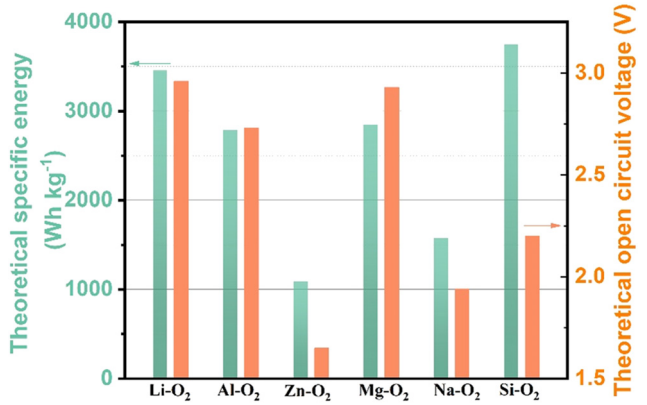

Fig. 1 The theoretical specific energy and open circuit voltage of various metal–air batteries. The specific energy is calculated by multiplying the theoretical specific capacity by the voltage.

Though LOBs hold great promise due to their high theoretical energy density, several crucial issues should be overcome to realize their real-world application. Specifically, the insulating discharged product of Li_2O_2 covered on the cathode surface blocks the diffusion pathway for oxygen and electrolyte ions, and leads to electrical passivation on the cathode, resulting in a large voltage hysteresis and limiting the capacity of LOBs, especially at high rates.[16] Reactive species generated during cycling give rise to electrolyte decomposition and electrode corrosion, and consequently terminate the cell life.[5]

The electrochemical performance and reaction pathways of LOBs are critically linked to the cathode design. Oxygen cathode materials should have a porous framework for O_2 diffusion and Li_2O_2 storage, superior catalytic activity, favorable ionic/electronic conductivity, electrochemical stability and nontoxicity.[20] Currently, noble metal materials such as Pt, Pd, IrO_2, and RuO_2 stand out as active electrocatalysts to address the sluggish kinetics of either the ORR or OER;[5,21] however, their high cost, scarcity, and inferior cycling stability hamper practical applications. Various nonprecious electrocatalysts like transition metal oxides,[11,13,16,17] metal carbides,[22–24] and perovskite oxides[25–27] have been investigated as cathode catalysts for LOBs. It should be noted that transition metal oxides possess relatively low electrical conductivity and poor stability,[28] and metal carbides have limited active sites because of the aggregation of metal particles. By contrast, perovskite oxides, a class of mixed-metal oxides, have a structural formula of ABO_3, where A is a lanthanide, alkaline or rare-earth cation, and B is a transition metallic element from the 3d, 4d or 5d configurations.[6,29–32] An ideal perovskite structure is a cubic structure, where the A cation has 12-fold coordination with O, while the B site resides in a corner-sharing octahedron of O anions (Fig. 2(b)).[33] More than 90% of metal cations in the periodic table can be accommodated in the framework of perovskites.[34] The crystal structure of perovskites is slightly different from that of spinel oxides (AB_2O_4), where A and B cations occupy tetrahedral and octahedral sites, respectively.[35] Owing to their distinct electronic, catalytic, and magnetic properties, perovskites have been applied in batteries and solar cells.[36–39] Their tunable compositions, crystalline structures, low cost and facile synthesis make them promising electrocatalysts for the ORR/OER. However, perovskite electrocatalysts,

Lulu Lyu

Lulu Lyu received her PhD (2021) from the Department of Convergence Science and Technology at Seoul National University. She is currently a research professor in Department of Materials Science and Engineering at Korea University. Her research focuses on nanomaterials and their applications for electrocatalysts and energy-storage materials.

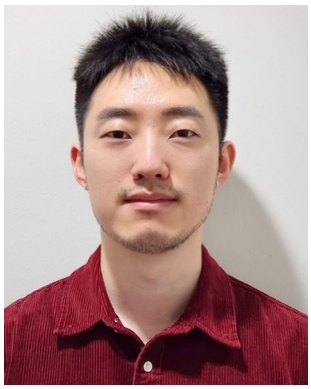

Seonyong Cho

Seonyong Cho is a PhD student in the department of materials science and engineering at Korea University under the supervision of Prof. Yong-Mook Kang. His research area is catalysts and system design for lithium–air batteries.

Yong-Mook Kang

Yong-Mook Kang completed his BS (1999), MS (2001), and PhD (2004) at Korea Advanced Institute of Science and Technology. He has been a senior researcher at Samsung SDI Co., Ltd. He is currently a professor at Department of Materials Science and Engineering in Korea University, Republic of Korea. His research area covers electrode or catalyst materials for rechargeable batteries. He has been appointed as RSC (Royal Society of Chemistry) fellow and representative of Korea from 2015 and a member of Y-KAST (Young Korean Academy of Science and Technology) from 2020.

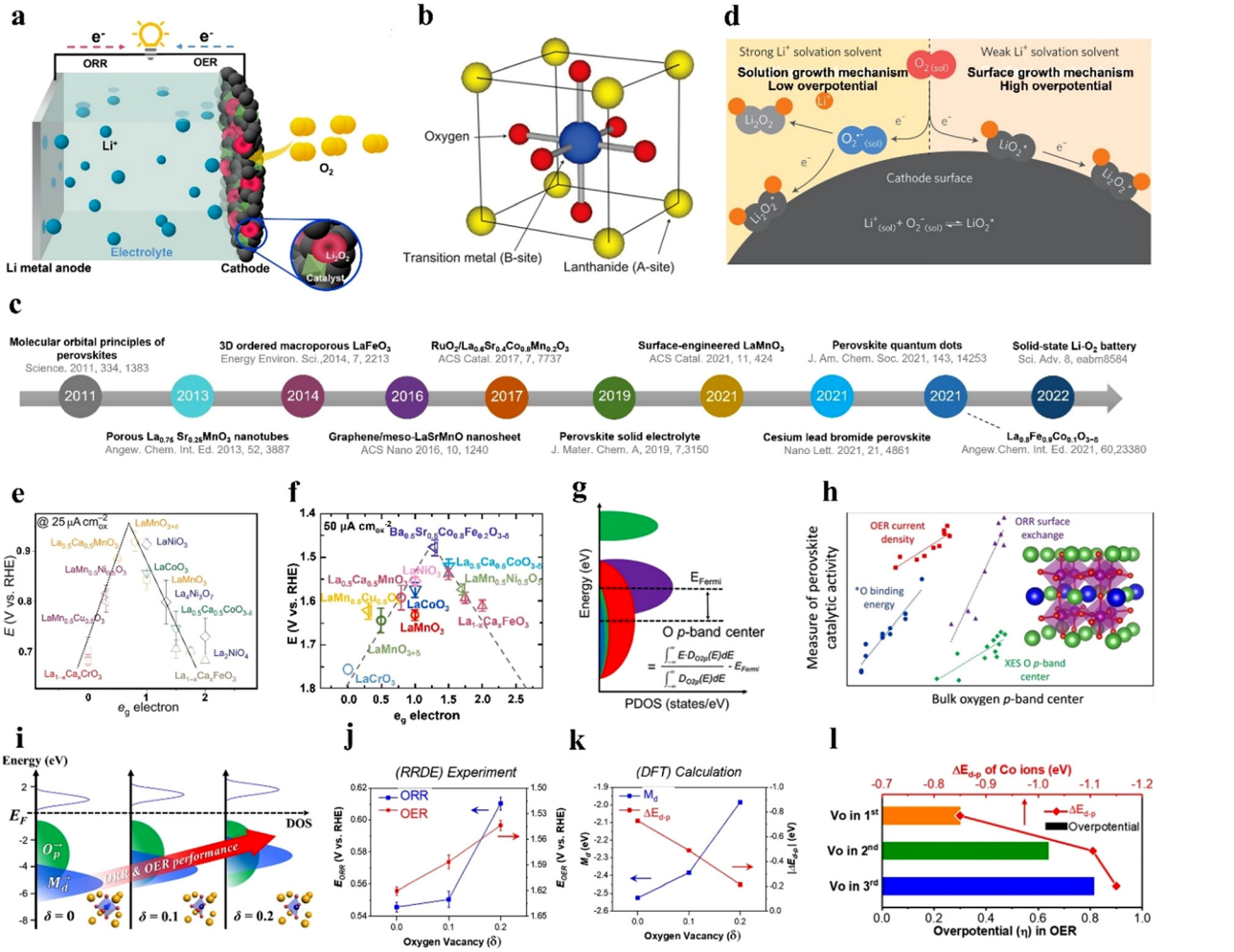

Fig. 2 Overview and mechanisms of LOBs, and descriptors for the catalytic activity of perovskite oxides. (a) Illustration of LOBs. (b) ABO_3 perovskite structure. (c) Timeline of research findings of perovskite oxides for LOBs. (d) Solution growth and surface-growth mechanisms in the LOB. Reproduced with permission.[49] Copyright 2016, Springer Nature. (e) Potentials as a function of e_g orbitals in perovskites. (b) and (e) Reproduced with permission.[33] Copyright 2011, Springer Nature. (f) OER performance as a function of the e_g orbital in perovskites. (g) Projected density of states (PDOS) of the O 2p orbit. (h) Catalytic activity as a function of the oxygen p-band center. (g) and (h) Reproduced with permission.[50] Copyright 2019, American Chemical Society. (i) The relationship between the electronic structure of $Sm_{0.5}Sr_{0.5}CoO_{3-\delta}$ and ORR/OER performance. (j) The relationship between ORR/OER activity and V_o based on experimental results. (k) The relationship between ΔE_{d-p}, M_d, and V_o based on DFT results. (l) Overpotential and ΔE_{d-p} values of the OER according to the V_o position in the 1st, 2nd, and 3rd layer of perovskites. (i)–(l) Reproduced with permission.[51] Copyright 2020, American Chemical Society.

when applied in non-aqueous LOBs, generally exhibit low Brunauer–Emmett–Teller (BET) surface areas, few morphologies and large particle sizes, which compromises their catalytic activity and the performance of LOBs.

The catalytic activity of perovskites can be flexibly tuned by several strategies. First, nanosizing bulk perovskites can expose enriched active sites and facilitate the diffusion of reactive species.[40,41] Second, substituting A-, B- and O-sites with foreign elements can change the electronic and crystal structures of the perovskites, thereby tuning the binding strength with oxygen intermediates.[42–44] Third, oxygen vacancies (V_o) can change the valence state of B-site cations and thus modulate the interaction between the metal ion and oxygen molecules.[45] Lastly, heterostructures combining perovskites with carbon materials, metal–organic frameworks (MOFs), and MXenes possess large surface areas, porous structures, and enhanced charge transfer efficiencies, which accommodate more LOB discharge products and increase the utilization of active sites.

The anticipated high energy efficiency, superior capacity, and long cycle life of LOBs are highly governed by the physicochemical properties of perovskite-based air cathodes. Even though review papers related to perovskite-based catalysts in aqueous solutions have been reported,[46–48] reviews that thoroughly outline recent advances in aprotic solutions for LOBs are rare. Hence, this review provides a timely and comprehensive understanding of recent advances towards perovskite catalysts for LOBs. Scheme 1 shows an overview of the perovskite-based electrocatalysts for LOBs in this review. Fig. 2(c) illustrates the timeline of the most impactful research findings related to perovskite oxides used for LOBs. Initially in

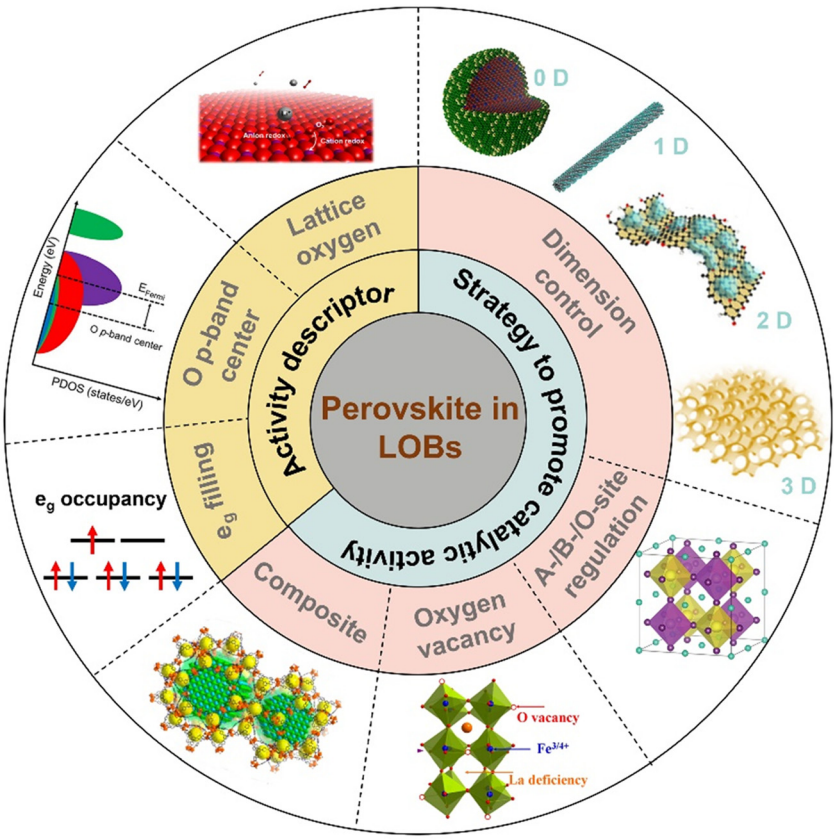

Scheme 1 Schematic illustration of perovskite oxides as cathodes for LOBs.

this mini-review, the energy-storage mechanisms of LOBs and the activity descriptors of perovskite oxides for the ORR/OER are demonstrated. Next, key strategies to boost the catalytic activity of perovskite oxides are described, including morphology and nanostructure control, A-/B-/O-site regulation, oxygen vacancies, and composites with other functional materials. Finally, a summary of the challenges and outlook of perovskite oxide electrocatalysts for LOBs is provided.

2. Mechanisms of LOBs

The growth and distribution of Li_2O_2 influences the reaction overpotential of an LOB. The electronic structures and morphologies of Li_2O_2 depend on solution growth (eqn (2)–(4)) or surface-growth mechanisms (eqn (5)–(7)), as shown in Fig. 2(d).[52] The two growth mechanisms are associated with the solubility of the LiO_2 intermediate. It has been reported that the donor number of the solvent can influence the solubility of LiO_2 and thus manipulates O_2 reduction pathways.[53]

Solution growth mechanism: O_2 molecules are reduced to superoxide (O_2^-), which dissolves into the electrolyte (expressed as $O_{2\,sol}^-$). Li^+ ions react with $O_{2\,sol}^-$ to generate soluble $LiO_{2\,sol}$. The $LiO_{2\,sol}$ intermediate in the electrolyte becomes Li_2O_2 after a disproportionation reaction.

$$O_2 + e^- \rightarrow O_{2\,sol}^- \quad (2)$$

$$Li^+ + O_{2\,sol}^- \rightarrow LiO_{2\,sol} \quad (3)$$

$$2LiO_{2\,sol} \rightarrow Li_2O_2 + O_2 \quad (4)$$

The solution-growth mechanism can be promoted by enhancing LiO_2 solubility in a high-donor-number-based electrolyte, generating toroidal Li_2O_2 made of lamellae and leading to a high discharge capacity. Due to the loose contact between Li_2O_2 and the catalyst and the low conductivity of the Li_2O_2 toroid, an LOB based on the solution-growth model exhibits a low round-trip efficiency and high charge overpotential despite its high specific capacity.[52,54] Moreover, a solvent with high polarity is easily affected by nucleophilic attack by O_2^-.[55] Efforts have been made to realize surface growth mechanisms by adding 2,5-di-*tert*-butyl-1,4-benzoquinone (DBBQ) in a low-donor-number solvent (LiTFSI in ether), where DBBQ avoided the direct formation of Li_2O_2 on the cathode surface.[55]

Surface growth mechanism: superoxide (O_2^-) adsorbs on the cathode surface to produce $O_{2\,sur}^-$ and then reacts with Li^+ ions from the electrolyte to generate $LiO_{2\,sur}$. $LiO_{2\,sur}$ is further reduced to generate Li_2O_2 by a $1e^-$ reduction step. The lower LiO_2 solubility in the surface growth pathway results in the generation of thin-film Li_2O_2 coating the surface, corresponding to a low capacity.

$$O_2 + e^- \rightarrow O_{2\,sur}^- \quad (5)$$

$$Li^+ + O_{2\,sur}^- \rightarrow LiO_{2\,sur} \quad (6)$$

$$LiO_{2\,sur} + Li^+ + e^- \rightarrow Li_2O_2 \quad (7)$$

3. Descriptors for the catalytic activity of perovskite oxides

3.1 e_g filling

Shao-Horn *et al.*[33] established an e_g-filling theory to disclose the fundamental mechanism of the ORR in ABO_3-type perovskites in alkaline solution. The d orbital of the central metal possesses two energy levels, namely, e_g and t_{2g} orbitals. Assuming that the surface transition metal center (B site) directly adsorbs O_2 molecules, the e_g orbital is predicted to overlap the O–$2p_\sigma$ orbital, and this overlap is stronger than that between the t_{2g} and O–$2p_\pi$ orbitals. Hence, compared to t_{2g}, e_g-filling of the B site is considered a more suitable indicator for the bonding strength between the B site and oxygen. Fig. 2(e) shows a volcano plot demonstrating the ORR activity of perovskites as a function of e_g-filling. A moderate amount of e_g-filling close to 1 promises the highest ORR performance. Low e_g-filling is predicted to result in strong B–O_2 bonding, and high e_g-filling in weak O_2 interaction. Likewise, the same group proposed that an e_g occupation close to 1.2 and a high metal–oxygen covalency in perovskites contribute to optimized OER activity.[32] Fig. 2(f) depicts OER activity as a function of the occupancy of the e_g-symmetry electron site of the transition metal cation. Shao–Horn's principle highlights that optimizing e_g filling is a feasible approach for the design of highly active perovskite catalysts, such as $LaCoO_3$,[40,56] $SrNb_{0.1}Co_{0.7}Fe_{0.2}O_{3-\delta}$,[57] $PrBa_{0.5}Sr_{0.5}Co_{1.5}Fe_{0.5}O_{5-\delta}$,[41] and $CaCu_3Fe_4O_{12}$.[58]

3.2 Oxygen p-band center

The oxygen p-band center (O_p) refers to the centroid of the PDOS of the O 2p orbit relative to the Fermi level (Fig. 2(g)), and is considered to be a bulk electronic structure descriptor for the evaluation of the catalytic activity of perovskites, based on density functional theory (DFT) calculations (Fig. 2(h)).[50] The gap value between the metal d-band center (M_d) and O_p, ΔE_{d-p}, is qualitatively associated with the bond hybridization of oxygen and the transition metal (TM). The strong hybridization between the metal 3d and O 2p orbitals positively affects the ORR/OER activity.[50] One study suggests that the concentration of V_o can influence both M_d and ΔE_{d-p} in $Sm_{0.5}Sr_{0.5}CoO_{3-\delta}$.[51] The increased V_o in $Sm_{0.5}Sr_{0.5}CoO_{3-\delta}$ decreases the coordination number and valence state of Co ($<4+$), further affecting the magnetic moment of the perovskite. The relationship between δ in $Sm_{0.5}Sr_{0.5}CoO_{3-\delta}$ and its electronic structure was revealed as an association between the V_o concentration and ORR/OER performance (Fig. 2(i)). Both experimental and DFT results suggest that the ORR can be enhanced by lifting the M_d close to the Fermi level, and OER can be boosted by decreasing ΔE_{d-p}, which can be tuned by the generation of V_o in the perovskite (Fig. 2(j) and (k)). Altogether, ORR and OER activity is strengthened by reducing ΔE_{d-p}, which can be realized by increasing M_d. More interestingly, the closer V_o is to the perovskite surface, the greater the promotion effect on catalytic activity (Fig. 2(l)). However, the fundamental mechanism of the ORR/OER of perovskites in a nonaqueous solution has not yet been fully understood.

3.3 Lattice oxygen

In addition to the B-site metal cationic redox contribution to the catalytic activity of perovskites, lattice oxygen on or near the perovskite surface is regarded as another redox pair that participates in the OER.[59–62] Grimaud *et al.*[60] predicted that when the O 2p orbit center moves up towards the Fermi level, the oxidation of lattice oxygen in perovskite oxides is thermodynamically favorable. Perovskite oxides with lattice-oxygen participation also demonstrate pH-dependent OER activity, implying a non-cooperative proton–electron transfer process.[60] Pan *et al.*[63] prepared Si-doped $SrCoO_{3-\delta}$ (Si-SCO), which showed better OER performance at different pH conditions than SCO (Fig. 3(a) and (b)). The lattice-oxygen oxidation mechanism (LOM) together with the adsorbate evolution mechanism (AEM) reaction pathways on Si-SCO are illustrated in Fig. 3(c), in which the LOM indicates that oxygen atoms on perovskites directly serve as active sites in the OER, and that AEM occurs through a concerted proton-coupled electron-transfer process on transition metal moieties. The contribution from the LOM to the OER activity of bulk perovskites was superior to that from the AEM. Notably, the influence of lattice oxygen from the perovskite surface resulted in a surface vacancy, and the generated vacant site was refilled by oxygen anions moving from the bulk material. The intrinsic OER activity was highly related to the diffusion rate of oxygen ions. A higher replenishment speed of surface lattice oxygen was responsible for a fast ion-diffusion rate, which benefited high OER activity (Fig. 3(d)). Si-SCO based on the LOM mechanism underwent surface reconstruction after cycling, as revealed by high-resolution transmission electron microscopy (HR-TEM) images (Fig. 3(e)), verifying the possible participation of lattice-oxygen redox.

In nonaqueous solutions, oxygen sites on the catalyst surface can directly interact with Li^+ ions from the electrolyte to generate surface Li sites, promoting the growth of Li_2O_2.[17] To illustrate the influence of both cation and anion redox on ORR/OER activity, our group prepared $LaMnO_3$ (LMO) perovskites with different surface atomic arrangements, namely, La-terminated or Mn-terminated surfaces (Fig. 3(f)).[61] The d band of the TM approached the Fermi-level in Mn-terminated LMO, while the O p band was near the Fermi-level in La-terminated LMO (Fig. 3(g) and (h)). Mn-terminated LMO involvement in both anion redox (surface lattice-O redox) and cation redox (TM redox) reactions resulted in the generation of a film-like discharge product. La-terminated LMO was inactive toward O_2 adsorption because of the nearly void d bands of the La sites, while the Mn-terminated surface actively adsorbed both O_2 and Li ions. Owing to the exposed lattice O from the stretched metal–oxygen bond and the presence of Mn^{3+} with a half-filled d band, the Mn-terminated LMO showed higher activity toward adsorbed O_2 than La-terminated LMO. Under air, the assembled LOB using an Mn-terminated LMO cathode exhibited superior performance than that using a La-terminated LMO (Fig. 3(i) and (j)).

Dynamic surface oxygen-involved reaction leads to an unstable surface, especially when the surface oxygen cannot

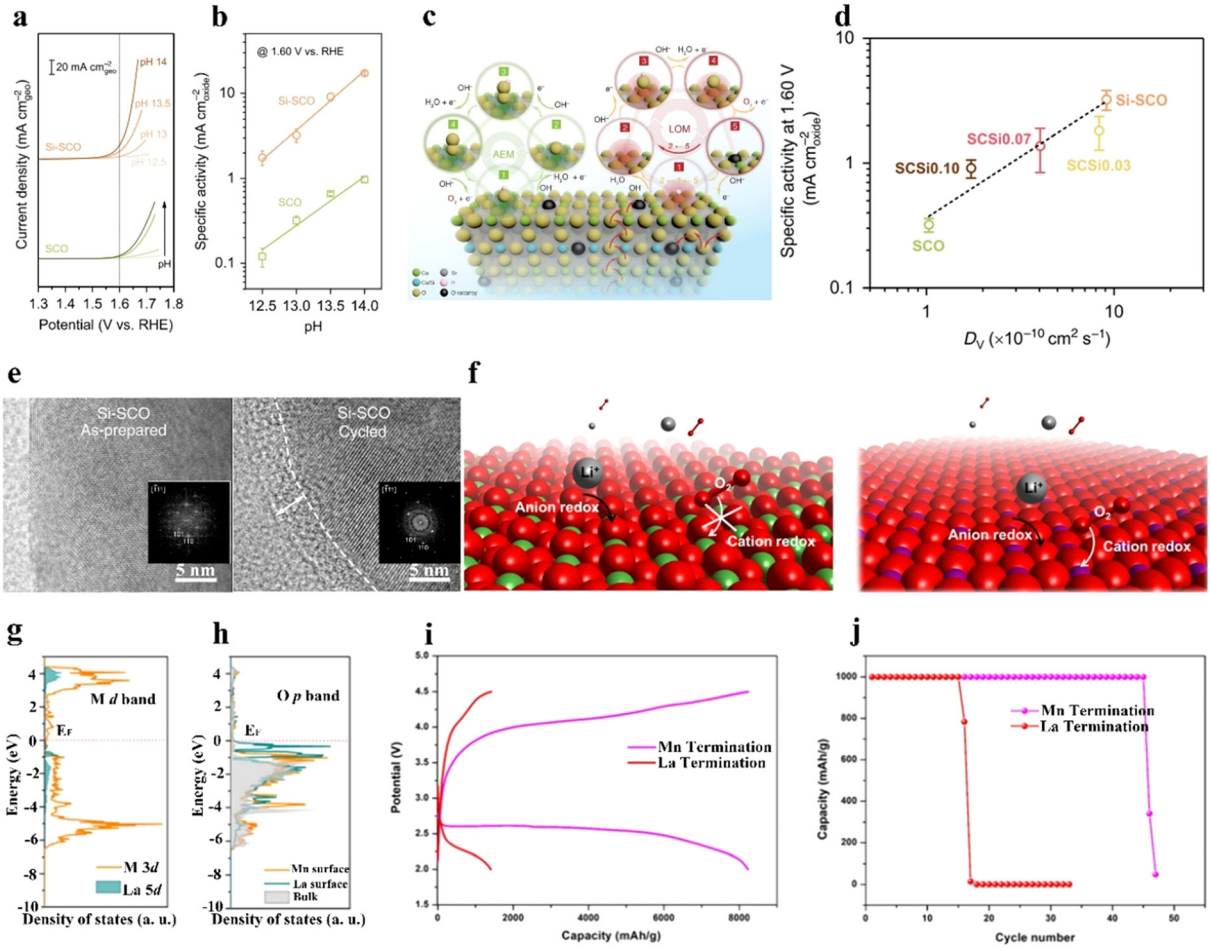

Fig. 3 Lattice oxygen on or near the perovskite surface to participate in the OER. (a) OER current density, and (b) specific activity of Si-doped SCO and SCO under different pH conditions. (c) Schematic illustration of the AEM and LOM mechanisms on Si-doped SCO. (d) The relationship between OER and the diffusion rate of V_O. (e) HR-TEM images of Si-SCO before and after cycling. Insets: Corresponding fast Fourier transformed patterns. (a)–(e) Reproduced with permission.[63] Copyright 2020, Springer Nature. (f) Illustration of reactions on La- and Mn-terminated $LaMnO_3$ surfaces. (g) The density of states of the Mn 3d and La 5d bands. (h) Oxygen 2p bands of Mn- and La-terminated $LaMnO_3$. (i) Discharge/charge curves at 200 mA g^{-1}. (j) Cycling stability of Mn- and La-terminated $LaMnO_3$ catalysts in a nonaqueous solution under air. (f)–(j) Reproduced with permission.[61] Copyright 2021, American Chemical Society.

be refilled by the bulk oxygen.[63–65] Hence, it is important to stabilize the perovskite surface to achieve high OER/ORR activity. Constant dissolution and deposition of catalysts during operando conditions may be a possible way to stabilize the catalyst surface, referred to as a self-healing process.[63]

4. Strategies for enhancing the catalytic activity of perovskites

Several tactics to promote the catalytic activity of perovskites are summarized in this mini-review, including dimensional control by synthetic methods, site substitution, oxygen vacancies, and perovskite-based composite catalysts. Table 1 lists the electrochemical performance and highlights of LOBs with perovskite cathodes.

4.1 Dimensional control by synthetic methods

Bulk perovskites show inferior stability and insufficient bifunctionality for the ORR/OER, giving rise to low specific capacities, poor rate capability, inferior round-trip efficiencies, and cycling instability. Nanosizing the bulk perovskites effectively enlarges the interfacial contact between the electrolyte and catalyst and exposes more active sites for the ORR/OER.[11,14,15,91] Various nanostructures and morphologies of perovskites have been fabricated, including nanocrystals,[66,92] 0D nanospheres,[75,83,86,93] 1D nanofibers/nanotubes,[25,71–73,78,82,94] 2D nanosheets,[76] 3D ordered structures,[85,95] and nanocubes.[96,97] This mini-review summarizes the research on small- and large-sized perovskite catalysts for LOBs in recent years.

4.1.1 Synthesis of small perovskites (<10 nm). When the size of bulk perovskites is reduced to the nanoscale, a host of active sites can be exposed to considerably boost catalytic activity, and the surface electronic structure of perovskites can be tailored. In addition, the adsorption energy of LiO_2 on the different facets of nanosized perovskite varies, which influences the OER performance.

$CsPbBr_3$ perovskite cubic nanocrystals (~8.5 nm) were prepared as catalysts for LOBs by a typical hot-injection strategy

Table 1 The electrochemical performance of LOBs with perovskite cathodes

Perovskite	Synthetic method	Structure	Specific capacity (mA h g^{-1} @mA g^{-1})	Overpotential (V@mA h g^{-1}@mA g^{-1})	Cycle life (cycles@mA h g^{-1}@mA g^{-1})	Highlights	Ref.
$CePbBr_3$	Hot-injection method	Cubic nanocrystal	7648@100		400@1000@500		66
$LaMnO_3$	Electrospinning	Nanofiber	18 000@200		100@1000@200	Collective anion and TM redox	61
$La_{0.7}MnO_{3-\delta}$	Sol–gel	Nanoparticle	29 286@50	0.38@1000@200	375@1000@300	A-site cationic defects	67
S-doped $LiNaO_3$	Sol–gel	Nanoparticle	24 067@100	0.37@1000@200	347@1000@100	Oxygen vacancy	68
$LaF_3/La_{0.8}Fe_{0.9}Co_{0.1}O_{3-\delta}$	Sol–gel	Nanoparticle	7373.5@100	1.29@500@200	157@500@200	F dopant	69
Ni-doped $LaNiO_3$	Sol–gel	Nanoparticle	5910@50	0.9@500@250	50@500@250	Oxygen vacancy	70
Oxygen-defective $CaMnO_3$	Sol–gel	Interconnected nanoparticle	3600@250	1.0@500@500	114@500@500	Redox mediator LiI; defects	45
$LaMn_{0.7}Co_{0.3}O_{3-\delta}$	Electrospinning	Nanofiber		0.81@1000@200	161@1000@200	1D nanotube structure	71
$La_{0.6}Ca_{0.4}Fe_{0.8}Ni0.2O_3$	Electrospinning	Nanotube	13 019@400		137@500@400	1D porous double-doped perovskite	72
$RuO_2@La_{0.6}Sr_{0.4}Co_{0.8}Mn_{0.2}O_3$	Electrospinning	RuO_2 nanosheets on nanofiber	12741.7@50	1.32@500@50	100@500@50	RuO_2/perovskite composite	73
$CoO/Sr_{0.9}Y_{0.1}CoO_{3-\delta}$	Electrospinning	Nanorod	3100@50		130@500@50	CoO/perovskite composite	25
$La_{0.8}Sr_{0.2}VO_3$	Electrospinning	Porous nanotube	5800@2000	1.16@1000@100	253@1000@2000	High reversibility under high current densities	42
$LaSrCoO/Ti_3C_2T_x$	Hydrothermal	Perovskite nanoparticle on 2D nanosheet	11 340@500	1.02@1000@500	80@1000@500	MXene/perovskite composite	27
$LaNi_{0.9}Co_{0.1}O_3$	Hydrothermal	Nanosheet		1.5@1000@0.1 mA cm^{-2}	100@1000@0.1 mA cm^{-2}	A binder-free electrode	74
$La_{0.8}Sr_{0.2}Co_{0.8}Fe_{0.2}O_{3-\delta}$	Sol–gel	Nanoparticle	26 833@50	0.55@1000@100	200@1000@300	Adjust metal–O covalency	43
$LaCo_{0.75}Mn_{0.25}O_{3-\delta}$	Hydrothermal	Hollow spherical structure	10 301@200	1.15@500@200	60@500@200	Tunable defect and surface structure	75
$LaFeO_{3-\delta}$	Sol–gel	2D nanosheet	14 983@100	1.2@1000@100	60@1000@100	Oxygen defects	76
$LaNi_{0.25}Co_{0.75}O_{3-\delta}$	Sol–gel	Interconnected nanoparticle	7720@0.1 mA cm^{-2}		49@1000	Ni dopant	77
$Ni_3S_2/PrBa_{0.5}Sr_{0.5}Co_2O_{5+\delta}$	Electrospinning & ALD	Ni_3S_2 nanoparticle on hollow perovskite nanofiber	12 874@100	0.68@1000@100	120@1000@100	Metal sulfide/perovskite composite	78
$Fe_2O_3/LaNiO_3$	Microwave & ALD	2D nanosheet	10 419@100	0.77@1000@100	90@500@100	Iron oxide/perovskite composite	79
$La_{0.6}Sr_{0.4}Co_{0.2}Fe_{0.8}O_{3-\delta}@Pd$	Wet chemistry	Nanoparticle	16 912@200		38@500@200	Pd/perovskite composite	80
$La_{0.8}Fe_{0.9}Co_{0.1}O_{3-\delta}$	Sol–gel	Nanoparticle	7270.1@100	0.7 V@500@200	215@500@500	Metal and alloy exsolution	81
$La_{0.75}Sr_{0.25}MnO_3$	Electrospinning	Porous nanotube	11 000@ 0.025 mA cm^{-2}		124@1000@0.15 mA cm^{-2}	Hollow 1D channels beneficial for electron transport and O_2 diffusion	82
Sr-doped-La_2NiO_4/NiO	Spray pyrolysis	Spherical particle	131 380@200	0.66@500@500	188@500@200	Sr dopant	83
$LaNi_{0.5}Co_{0.5}O_3$	Sol–gel	Spherical nanoparticle	7.96 mA h cm^{-2}@ 0.1 mA cm^{-2}	0.05@0.5 mA cm^{-2}@0.1 mA cm^{-2}	100@0.5 mA cm^{-2}@0.1 mA cm^{-2}	98.2% energy efficiency LOB	84
$LaFeO_{3-\delta}$	Emulsion polymerization & Annealing	3D ordered macroporous honeycomb	15 000@0.025		124@1000@0.15 mA cm^{-2}	3D ordered macroporous structure	85
$La_{0.6}Sr_{0.4}CoO_{3-\delta}$	Hydrothermal & template method	Macrosphere	4895@100	1.06@100(non-capacity limit)	30@500@0.1 mA cm^{-2}	Catalytic activity in both aqueous and non-aqueous solution	86
$RuO_2/La_2LiRuO_{6-\delta}$	Ball milling	Nanoparticle		0.9@100@10 mA g_{carbon}^{-2}	665@200@100	Solid-state LOB	38
$Ag@La_{0.6}Sr_{0.4}Fe_{0.9}Mn_{0.1}O_3$	Sol–gel & UV irradiation	Nanoparticle	12 477	1.3@500@400	147@500@400	Ag/perovskite composite	87
$Ni\text{-}La_{0.9}Mn_{0.6}Ni_{0.4}O_{3-\delta}$	Electrospinning	Nanoparticles on nanofiber	16 656@400		95@500@400	Exsolution of Ni nanoparticles	88
$LaCo_{0.8}Fe_{0.2}O_3@rGO$	Hydrothermal	Nanowire on rGO sheet	7088.2@200	0.98@500@200	56@500@200	rGO/perovskite composite	89
$\alpha\text{-}Fe_2O_3/La_{0.8}FeO_{3-\delta}$	Sol–gel	Nanoparticle	7183@100	1.0@500@100	108@500@100	Fe_2O_3/perovskite composite	90

Note: rGO: reduced graphene oxide.

(Fig. 4(a) and (b)).[66] During charging, the decomposition of Li_2O_2 in the $CsPbBr_3$ nanocrystals followed two steps: (1) $Li_2O_2 = LiO_2 + Li^+ + e^-$ and (2) $LiO_2 = O_2 + Li^+ + e^-$ (rate-determining step), as shown in Fig. 4(c). The (100) facet displayed the smallest adsorption energy toward LiO_2 compared to the (110), (210), (211), and (321) facets, resulting in a small overpotential for the OER. For the ORR process, LiO_2 preferentially dissolved in the electrolyte and produced the toroid-type Li_2O_2 based on the solution growth mechanism (Fig. 4(d)). Additionally, $CsPbBr_3$ perovskite quantum dots (4–5 nm) were deposited into an iron-based metal–organic framework in organic solvent *via* a sequential deposition method, named $CsPbBr_3$@PCN-333(Fe) (Fig. 4(e) and (f)).[92] Oleic acid and oleylamine were added to the mixture as organic stabilizers. The composite was applied as a photoelectric cathode for a light-assisted LOB. The LOB using the $CsPbBr_3$@PCN-333(Fe) cathode retained a higher discharge voltage (2.5 V at 0.5 mA cm^{-2}) than $CsPbBr_3$ (<2 V) and PCN-333(Fe) (2.4 V) (Fig. 4(g)).

4.1.2 Synthesis of large perovskites

Sol–gel. Sol–gel is a facile synthetic method used to prepare perovskite nanomaterials based on the inorganic polymerization reaction of molecular precursors.[26,43,45,67–70,84,98–100] First, different metal nitrates or acetates with specific stoichiometric

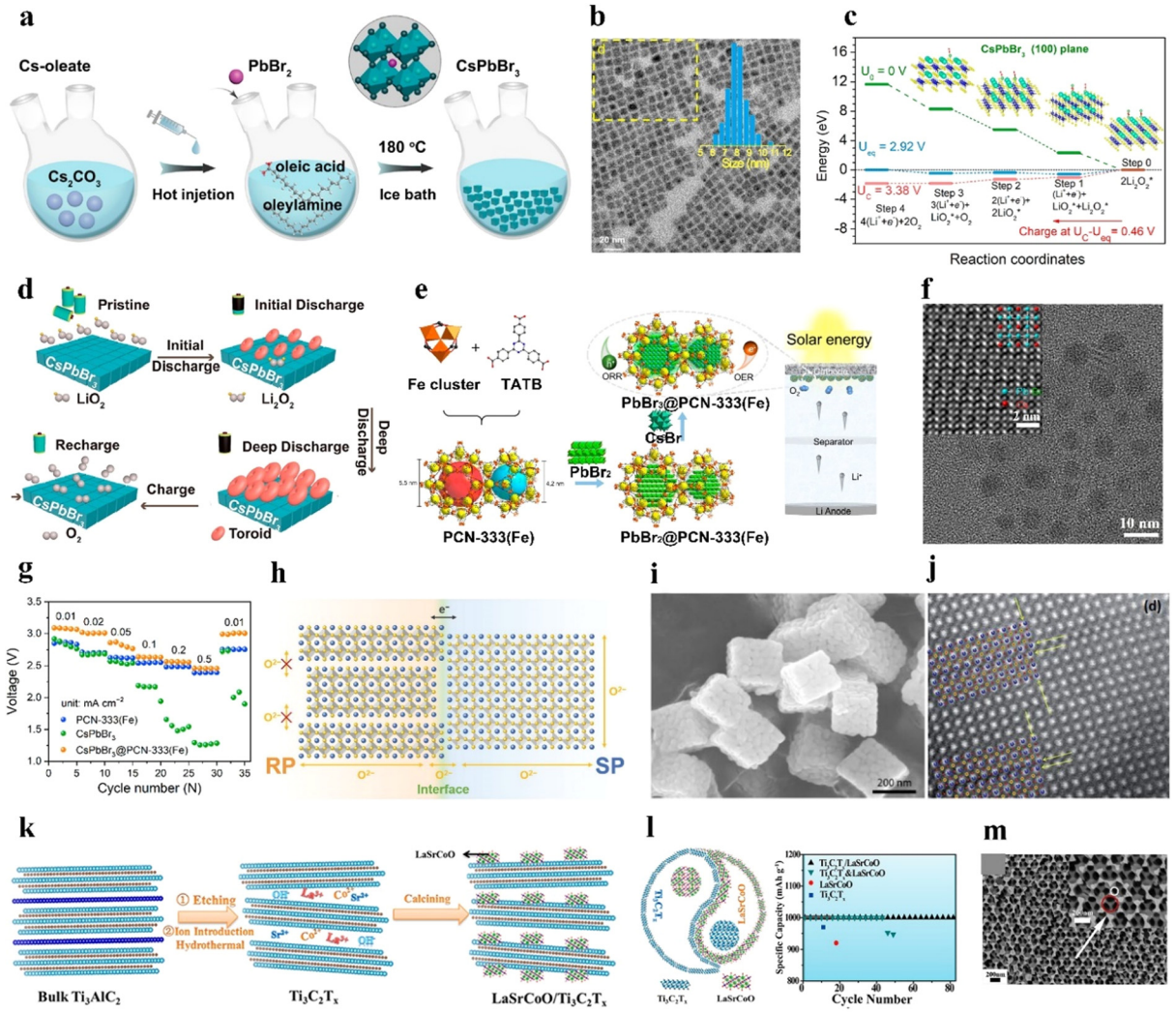

Fig. 4 Synthesis of large perovskites. (a) Illustration of the synthesis process of $CsPbBr_3$ nanocrystals. (b) Transmission electron microscopy (TEM) image of $CsPbBr_3$ nanocrystals. (c) Gibbs free energy at different potentials of $CsPbBr_3$. (d) Demonstration of discharging/charging processes for LOBs with $CsPbBr_3$. (a)–(d) Reproduced with permission.[66] Copyright 2021, American Chemical Society. (e) Preparation process of $CsPbBr_3$@PCN-333(Fe). (f) TEM image of $CsPbBr_3$@PCN-333(Fe). (g) Variation of discharge voltage at distinct current densities with $CsPbBr_3$@PCN-333(Fe) and control samples under illumination. (e)–(g) Reproduced with permission.[92] Copyright 2021, American Chemical Society. (h) Demonstration of the possible electron and oxygen–ion transfer at the interface of dual phases in $LaSr_{3-y}$. Reproduced with permission.[101] Copyright 2021, Wiley-VCH. (i) Scanning electron microscopy (SEM) image of $La_{0.9}Co0.8Ni_{0.2}O_{3-x}$ nanocubes. Reproduced with permission.[97] Copyright 2019, Elsevier. (j) Scanning TEM image of $LaNi_{0.9}Cu_{0.1}O_3$ with crystal strains. Reproduced with permission.[74] Copyright 2017, Royal Society of Chemistry. (k) Illustration of the synthesis process of the LaSrCoO/$Ti_3C_2T_x$ composite. (l) Cycling stability of LaSrCoO/$Ti_3C_2T_x$. Reproduced with permission.[27] Copyright 2019, American Chemical Society. (m) SEM image of macroporous $LaMnO_3$. Reproduced with permission.[95] Copyright 2019, Elsevier.

ratios are dissolved in deionized water, followed by adding chelating agents (*e.g.*, ethylenediamine tetraacetic acid and citrate acid) and binding agents (like ethylene glycol). An NH_4OH solution is added to the above mixture to adjust the pH of the mixture to 6–8, allowing complete complexation. Then, the mixture is aged at 80–120 °C to form a gel. The gel is further dried below 300 °C to generate a fluffy resultant, followed by high-temperature annealing (above 600 °C) under air to remove organic moieties. The sol–gel approach combined with ultraviolet light was used to place Ag nanoparticles on $La_{0.6}Sr_{0.4}Fe_{0.9}Mn_{0.1}O_3$ with a BET specific surface area (SSA) of 20.83 $m^2\ g^{-1}$. The derived LOB exhibited a superior capacity (12 477 mA h g^{-1} at 400 mA g^{-1}) and a long cycle life (147 cycles under a limited capacity of 500 mA h g^{-1} at 400 mA g^{-1}).[87]

V_o can be created by annealing the perovskite product derived from the sol–gel under a reducing atmosphere such as an H_2/Ar mixed atmosphere.[45] Zhu *et al.*[100] prepared $La_{1-x}FeO_{3-\delta}$ perovskites with surface V_o and a small portion of Fe^{4+} species, as bifunctional ORR/OER catalysts by an EDTA–citrate complexing sol–gel process. In addition, Xu *et al.*[101] used a sol–gel method to prepare cation-deficient $LaSr_{3-y}$ with dual phases of Ruddlesden–Popper perovskite (RP) and single perovskite (SP) with controllable structures and compositions. The interfacial interaction of the perovskite composite elevated the oxygen and ionic transport, which enhanced the lattice-O participation in the OER process in an alkaline electrolyte (Fig. 4(h)).

Oxygen in sol–gel derived perovskite oxides can be replaced by N, S, and F, which is realized by placing anion precursors and the perovskite oxide in two separated porcelain boats in a tube furnace, followed by heating at around 300–400 °C under an Ar atmosphere.[68,69] In short, the sol–gel method allows flexibility in the construction of various perovskites. However, perovskite oxides prepared by this method generally possess a low BET surface area ($<50\ m^2\ g^{-1}$), unfavorable for electrolyte diffusion and limiting the number of exposed active sites.

Electrospinning. 1D perovskite nanofibers with high surface-to-volume ratios show a relatively large surface area and well-distributed porosity, which maximizes the electrolyte-accessible active sites, facilitates mass transport, accommodates reaction products, and mitigates the clogging issue on the catalyst surface. An electrospinning method has been widely adopted to prepare 1D porous perovskite nanomaterials, such as $La_{0.6}Ca_{0.4}Fe_{0.8}Ni_{0.2}O_3$, $LaMn_{0.7}Co_{0.3}O_{3-x}$ nanotubes, $PrBa_{0.5}Sr_{0.5}Co_{2-x}Fe_xO_{5+\delta}$ nanofibers, $La_{0.6}Sr_{0.4}Co_{0.8}Mn_{0.2}O_3$ nanofibers, $Sr_{0.9}Y_{0.1}CoO_{3-\delta}$ nanorods, and $La_{0.8}Sr_{0.2}VO_3$ nanofibers.[25,42,71–73,102] First, one or more metal precursors are dissolved in organic solvent and mixed with polymer solutions like polyacrylonitrile and polyvinylpyrrolidone (PVP) to generate the mother solution. Then, the mixture is filled into a plastic syringe tube equipped with a stainless-steel nozzle. The solution is electrospun onto a rotating drum, as a collector, under a high voltage. Thereafter, the collected nanofibers are stabilized and pyrolyzed in a muffle oven or tube furnace.

The morphology and porous structure of the electrospinning products can be tailored using different amounts of polymer precursors during electrospinning. As such, Wang *et al.*[72] demonstrated that adjusting the concentration of PVP changed the morphology of $La_{0.6}Ca_{0.4}Fe_{0.8}Ni_{0.2}O_3$ from nanofiber to nanotube. A low concentration of PVP, around 0.13 g mL^{-1}, resulted in the formation of hollow nanotubes with a diameter of 100–200 nm, while a higher-concentration of PVP of around 0.18 g mL^{-1} generated solid nanofibers after calcination. When PVP was present in a low amount, it preferentially lied at the perovskite core to form a hollow structure. Although, the metal composition, morphology and porous structure of the resultant can be tuned by adopting various precursor components and annealing temperatures, the distribution of multi-scale pores cannot be realized by the electrospinning technique.

Hydrothermal. A hydrothermal method has been used to prepare perovskites or their composites as effective catalysts for LOBs.[27,74,97] Sun *et al.*[97] prepared porous $La_{0.9}Co0.8Ni_{0.2}O_{3-x}$ nanocubes by a hydrothermal method in the presence of PVP and glycine. The nanocubes had a larger BET surface area (23.45 $m^2\ g^{-1}$) than that of the sample prepared by the sol–gel process (4.82 $m^2\ g^{-1}$) (Fig. 4(i)). PVP and glycine, as a potential crystal face inhibitor and shape-control agent, respectively, were applied to produce the cube-like framework.

A binder-free electrode is conducive for effective electron transfer. As such, $LaNi_{0.9}M_{0.1}O_3$ (M: Cu or Co) perovskite nanosheets were deposited on 3D Ni foam by a hydrothermal method as self-standing air electrodes for LOBs, and the derived sample exhibited an SSA of 240 $m^2\ g^{-1}$.[74] Substituting Ni^{3+} with Cu^{2+} increased the crystalline plate distance and generated V_o. Crystal strain and dislocation defects can be observed in $LaNi_{0.9}Cu_{0.1}O_3$ (Fig. 4(j)), attributed to the substitution with a TM ion of a different size, as well as the formation of V_o induced by the different chemical valence of the metal ions. Due to the microporous structure of the $LaNi_{0.9}Cu_{0.1}O_3$ catalyst and the use of a redox mediator (tetrathiafulvalene), the derived LOB exhibited a small overpotential of 0.72 V and high round-trip efficiency. Li_2O_2 was uniformly deposited on the catalyst nanosheet during the discharge process and then decomposed after the charging process. Moreover, $La_{0.5}Sr_{0.5}CoO_{3-\delta}$ (LaSrCoO) nanoparticles were deposited in $Ti_3C_2T_x$ nanosheets by hydrothermal and post-thermal treatment (Fig. 4(k)).[27] The LaSrCoO/$Ti_3C_2T_x$ composite showed longer cycle life compared to LaSrCoO and $Ti_3C_2T_x$ due to the synergistic effect of the dual components (Fig. 4(l)).

Since solid discharge products deposit on the surface of the catalysts, a porous structure of catalyst is essential for improving the electrochemical performance of LOBs. Macropores provide sufficient space for efficient mass diffusion (Li^+ ions and O_2), allowing fast ORR/OER kinetics. Mesoporous channels can trap the Li_2O_2 discharge product and prevent it from diffusing into the electrolyte, ensuring favorable interfacial contact between Li_2O_2 and the catalyst and thus lowering the reaction overpotentials.[54] Hard template synthesis,[83,95] a soft-template route,[76] and wet-chemistry[80] have been used to

prepare porous perovskites. Ordered macroporous $LaMnO_3$ with an SSA of 20.3 $m^2\ g^{-1}$ was prepared using PMMA colloidal crystals as a hard template, facilitating both oxygen and electrolyte diffusion (Fig. 4(m)).[95] However, only a few reports investigate how the porous structure and porosity influence the catalytic activity of perovskites for LOBs. Hence, more efforts are needed to investigate the property–activity relationship of perovskite catalysts.

4.2 A-/B-/O-site regulation in ABO_3

4.2.1 A-site cation deficiency. A-/B-site cations can be substituted for other cations with different valences or radii. The adjustment of A-site cation size influences the chemical balance state of ABO_3, and results in the octahedron distortion in the initial cubic framework, generating cation vacancies or oxygen vacancies.[47] Owing to their unique structures, perovskites with diverse compositions demonstrate varying redox and surface properties. The order of ORR performance of ABO_3 perovskites with disparate rare-earth metals as A-site elements was demonstrated to be La > Pr > Nd > Sm > Gd > Y > Dy > Yb.[103]

Perovskites with A-site vacancies can be prepared by a nonstoichiometric method. Du *et al.*[67] produced La defects in $La_{0.7}MnO_{3-\delta}$ ($L_{0.7}MO$) as a bifunctional catalyst for the OER/ORR by decreasing the stoichiometric ratio of $La(NO_3)_3{\cdot}6H_2O$ in the sol–gel synthesis. The defective sample possessed a larger BET surface area (34.7 $m^2\ g^{-1}$) and pore size (20.6 nm) than that of the defective-free sample (11.9 $m^2\ g^{-1}$, 8.9 nm), beneficial for oxygen and Li^+ transport and the storage of Li_2O_2. The generated La defects effectively elevated the Mn–O bond covalency, which optimized the e_g electron filling state of the Mn ions and improved the overlapping status of Mn 3d and O 2p orbitals. Furthermore, La defects on the $L_{0.7}MO$ surface served as multiple unsaturated active spots to adsorb oxygen intermediates, leading to strong interaction between the catalyst and LiO_2. Thereafter, the adsorbed LiO_2 underwent a one-electron transfer reaction to generate a film-like Li_2O_2 uniform covering on the catalyst surface, which corresponded to a surface growth mechanism. As a result, lattice-oxygen redox reactions and electron transfer in $La_{0.7}MnO_{3-\delta}$ were accelerated between Mn and oxygen adsorbates. The LOB using $L_{0.7}MO$ delivered a superior capacity of 29 286 mA h g^{-1} at a current density of 50 mA g^{-1} (compared with 13 709 mA h g^{-1} from the cell using a defective-free sample), a small voltage gap (0.38 V) and stable cycling life (375 cycles under a confined capacity of 1000 mA h g^{-1} at 300 mA g^{-1}).

4.2.2 B-site substitution. The multiple oxidation states of the B site enable perovskites with tailorable surface redox properties, allowing their catalytic activity for chemical reduction or oxidation. B-site cations directly bond with oxygen-related adsorbates, and the degree of B–O_2 covalency can be altered by substituting the B-site with foreign cations. The radius, alkalinity or acidity, oxidation valence, and spin state of B-site metal ions impact the physicochemical properties and stability of the resulting perovskite.[47] Moreover, the oxidation state and spin state of B-site cations can greatly influence their e_g electronic state.[100]

Owing to the overlap between B-site ions and the O^{2-} orbital, the electronic conductivity is governed by B–O–B bonds and the valence transition of the B cations.[47] A shorter B–B distance is conducive to the formation of O–O bonds between the neighboring adsorbates, beneficial for OER kinetics.[104] A shorter B–B bond in ABO_3 and a smaller B–O–B angle can be realized by foreign-cation doping.[105] As such, doping a Co element into $LaMn_{0.7}Co_{0.3}O_{3-x}$ nanotubes shortened the Mn–Mn distance and promoted the formation of O–O bonds, favorable for promoting the OER performance.[71] The assembled LOB could be operated for 161 cycles with a confined capacity of 1000 mA h g^{-1} at 200 mA g^{-1}.

Furthermore, the oxidation state of the B-site TM and the amount of V_o can be regulated by foreign-cation doping, providing a versatile way to correlate physicochemical features with catalytic activity. The presence of aliovalent dopants results in the generation of a positively charged V_o to maintain charge neutrality based on Coulomb's law. Defective perovskite structures assist in the migration, emission, and intercalation of lattice oxygen, thereby enhancing the redox capability of B-site cations. For example, the introduction of Sr decreases the valence state of the B-site metal and the crystallinity structure.[42] Sung *et al.*[42] induced a phase transition from $La_{0.8}Sr_{0.2}VO_4$ monazite (LSV4) to $La_{0.8}Sr_{0.2}VO_3$ perovskite (LSV3) under a reducing atmosphere (Fig. 5(a)). LSV3 showed a defective and porous structure, strain and lattice shrinkage induced by mismatching of VO_6 octahedra (Fig. 5(b)). The reduced oxidation state from V^{5+} to V^{3+} induced by the Sr dopant allowed the generation of enriched V_o active sites. LSV3 exhibited better ORR and OER performance (Fig. 5(c) and (d)), conducive to the formation and decomposition of Li_2O_2. Accordingly, the assembled LOB demonstrated high reversibility over 253 cycles with a limited capacity of 1000 mA h g^{-1} at 2000 mA g^{-1} and stable rate capabilities at different current densities from 100 to 2000 mA g^{-1} (Fig. 5(e)).

In $LaCoO_3$, partial replacement of the Co site in the B-site with Mn or Fe can boost the rate kinetics and coulombic efficiency and elongate the cycle life of the resulting LOB. Abundant V_o in mesoporous $LaCo_{0.75}Mn_{0.25}O_{3-\sigma}$ (LCMO) effectively bound the intermediate product of $Li_{2-x}O_2$, accelerated electron transfer, and lowered the reaction energy barrier.[75] Accordingly, the LOB using an LCMO cathode exhibited a low potential of 1.12 V and a high specific capacity of 10 301 mA h g^{-1} at 200 mA g^{-1}. In another example, the doping effect of different cations like Mn and Fe in the catalytic activity of $La_{0.6}Sr_{0.4}CoO_3$ was compared (Fig. 5(f)).[106] The Fe dopant was effective in reducing the grain size of the perovskite nanoparticles, leading to a higher SSA (10.69 $m^2\ g^{-1}$) than that of the pristine sample (6.68 $m^2\ g^{-1}$) and thus exposing more active sites. Moreover, the introduced Fe^{2+} contributed to generating more V_o, according to $Fe_{Fe}^{\times} + O_O^{\times} \leftrightarrow Fe_{Fe}' + V_O^{\bullet} + \frac{1}{2}O_2$. Mn possessed a mixed valence between $2^+/3^+$ and $3^+/4^+$, and exhibited an electron-donating feature. Thus, the electron-rich Mn-doped

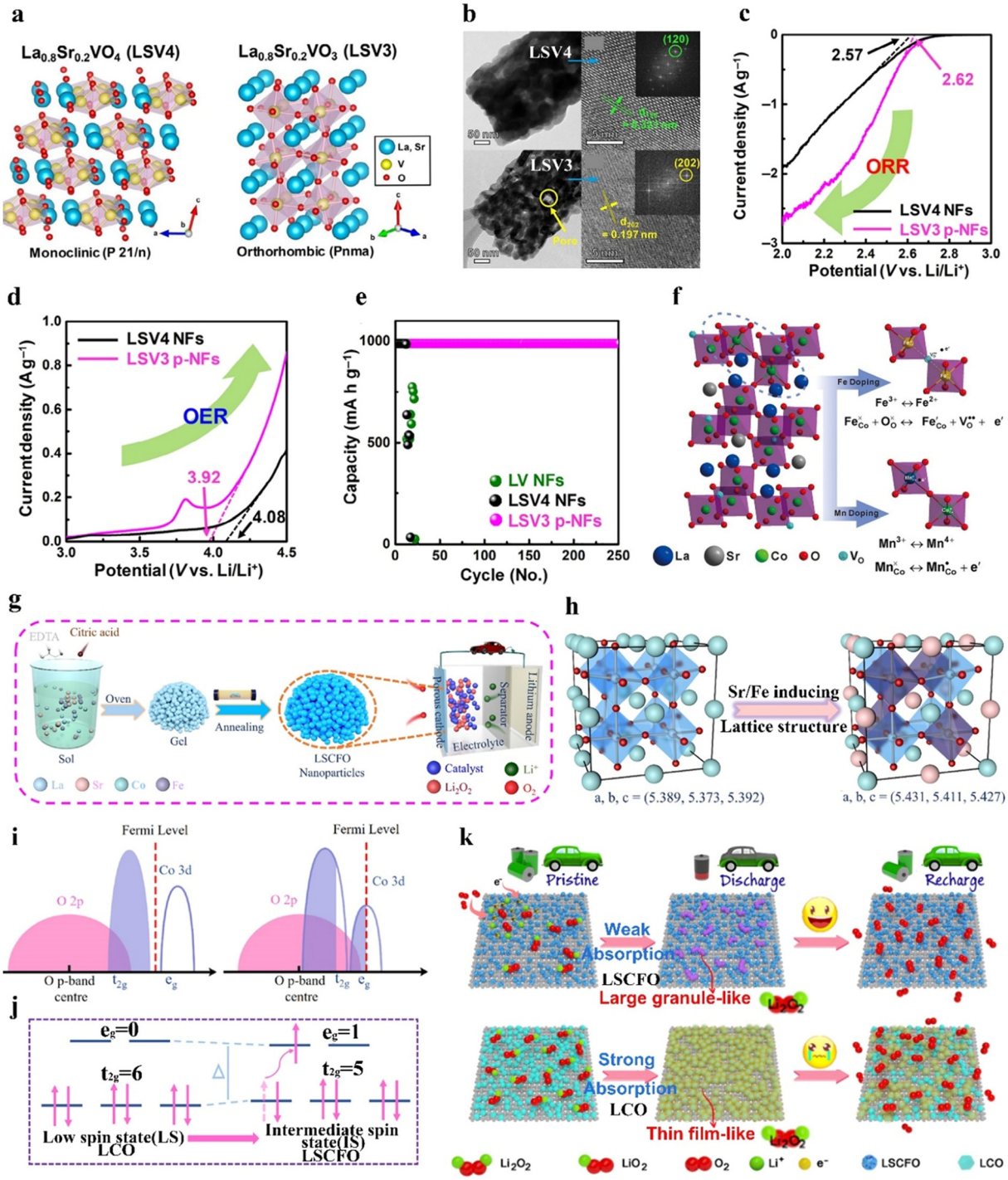

Fig. 5 The impact of B-site substitution on perovskites. (a) Crystal structures of LSV4 and LSV3. (b) Low- and high-resolution TEM images of LSV4 and LSV3. (c) ORR and (d) OER linear sweep voltammetry of LSV4 and LSV3 at 5 mV s^{-1}. (e) Cycling stability of LOBs with LSV4 and LSV3 catalysts. (a)–(e) Reproduced with permission.[42] Copyright 2021, Wiley-VCH. (f) Demonstration of the Fe and Mn dopants in $La_{0.6}Sr_{0.4}CoO_3$. Reproduced with permission.[106] Copyright 2018, Wiley-VCH. (g) Schematic illustration of the preparation of LSCFO. (h) Crystal structures, and (i) the overlapping state of the Co 3d–O 2p bonds of LCO and LSCFO. (j) Schematic illustration of the spin state transformation from LCO to LSCFO. (k) Illustration of the oxygen electrode reaction pathways of LCO and LSCFO. (g)–(k) Reproduced with permission.[43] Copyright 2021, American Chemical Society.

sample increased the electrical conductivity, which was beneficial for electron transfer during the ORR/OER. Mn and Fe dopants with larger radii than Co can expand the crystalline structure, and thus create more pathways for Li^+ transport. In addition to a TM dopant, a magnesium dopant in $LaNi_{1-x}Mg_xO_3$ has been introduced to replace Ni, and this suppressed the formation of low-valence Ni^{2+} ions ($e_g > 1$). The presence of Ni^{3+} ($e_g = 1$) in the Mg-doped sample ensured

high ORR/OER activity.[107] The derived LOB with the Mg-doped cathode demonstrated a higher discharge capacity than that using the pristine sample.

Dual cation dopants in ABO_3 perovskites can synergistically regulate the adsorption capability of catalysts toward the LiO_2 intermediate and the morphology of the discharge product. $LaCoO_3$ (LCO) is a nonmagnetic insulator due to the low-spin state of Co^{3+} with an atomic configuration of $t_{2g}^6e_g^0$.[43] Sr and Fe cations doped in porous $LaCoO_3$ perovskite nanoparticles (LSCFO) by a sol–gel method resulted in the formation of abundant V_o and enhanced Co 3d–O 2p covalency bonds, and induced the transformation of Co^{3+} from a low-spin state to an intermediate-spin state (Fig. 5(g)–(j)).[43] The enhanced Co 3d–O 2p covalency facilitated electron transfer between the surface TM and adsorbed intermediates, and the optimized spin state transformed the perovskite from a nonconductor state to a metallic state. Hence, the produced granule-like Li_2O_2 in LSCFO can be more effectively decomposed during the charging process, compared to LCO (Fig. 5(k)). This LOB device demonstrated long-term cycling stability over 200 cycles at 300 mA g^{-1}, and an ultrahigh specific capacity of 26 833 mA h g^{-1} at 50 mA g^{-1}. Moreover, Cu with a low valence state and Co with a favorable $4e^-$ process were also co-doped to $LaMnO_3$ by gel combustion to promote ORR/OER activity.[108]

4.2.3 O-site substitution. Substituting the oxygen in ABO_3 perovskites by anions with relatively low Pauling electronegativity effectively strengthens the covalent characteristics of metal–anion bonds, thus reducing the bandgap. The decreased bandgap excites charge carriers to the conduction band, considerably boosting electronic conductivity. A sulfur dopant in perovskites contributes to the strengthened hybridization of the 3d orbital of the B-site cation and the 2p orbital of the O, which reinforces the bond strength and thereby boosts the catalytic kinetics.[68,109,110] For example, Long *et al.*[68] synthesized S-doped and O-defective $LiNiO_3$ (S-V_o-LNO) with a narrow bandgap, and increased the electron-occupied state to nearer the Fermi level than in the pristine LNO. Furthermore, the upshift of the Ni 3d band center and downshift of the O 2p band center led to a smaller distance between them (Fig. 6(a)). The strengthened hybridization of Ni 3d and O 2p orbitals and the promoted Ni–O covalency boosted the electron transfer. In addition, Ni^{3+} with an optimal e_g orbital ($t_{2g}^6e_g^1$) was predicted to have a higher catalytic activity than that of Ni^{2+} ($t_{2g}^6e_g^2$) according to e_g-filling theory. A higher amount of Ni^{3+} in S-V_o-LNO compared to that in LNO increased the adsorption strength of oxygen intermediates on the surface and reduced the reaction energy barrier during the OER and ORR (Fig. 6(b) and (c)). The discharge products, Li_2O_2 and Li_2CO_3, could be effectively decomposed on the surface of S-LNO after recharging, while they remained on the LNO surface. Consequently, the LOB using the S-LNO cathode exhibited a superior capacity of 24 067 mA h g^{-1} at 100 mA g^{-1}, low overpotential (0.37 V), favorable rate capability, and long cycle life (347 cycles with a limited capacity of 1000 mA h g^{-1} at 100 mA g^{-1}) (Fig. 6(d) and (f)).

Regulating the morphology and composition of the discharge product Li_2O_2 is a feasible way to improve the performance of LOBs, and can be realized by anion doping in perovskites. Using fluorine, the dopant with the highest electronegativity (4.0), can improve the electronic conductivity of electrocatalysts and generate V_o by forming metal–F bonds. As shown in Fig. 6(g), Hou *et al.*[69] introduced an F dopant into $La_{0.8}Fe_{0.9}Co_{0.1}O_{3-\delta}$ (LFCO), reconstructing the surface property, manipulating the electronic structure, and tailoring the discharge reaction pathway of the LOB. The F dopant distorted the crystalline structure, increased the disorder degree in the adjacent environment of the Fe–O bond, and tailored the Fe/Co–O orbital hybridization. Based on theoretical calculations, due to the strong LiO_2 adsorption energy in the derived LaF_3/LFCO composite, the discharge reaction process on the cathode followed the surface growth mechanism. In this context, LiO_2 may not transport to the electrolyte and may instead favor the formation of small-sized Li_2O_2 (0.2 μm) in LaF_3/LFCO, while the sample without F demonstrates larger-sized Li_2O_2 (2 μm) that leads to a larger overpotential (Fig. 6(h) and (i)). The generated petal-like F-doped Li_2O_2 shows better electrical conductivity and smaller charge transfer resistance, beneficial for lowering the overpotential (1.29 V) and enhancing the cycling stability of LOB (157 cycles with a limited capacity of 500 mA h g^{-1} at 200 mA g^{-1}).

A nitrogen dopant with an analogous atomic size to O and lower ionization energy could induce the formation of V_o because of charge balancing. Zhang *et al.*[70] synthesized N-doped $LaNiO_3$ (LNO) with an increased amount of V_o and Ni^{3+}. Ni^{3+} with its optimized e_g-filling orbital ($t_{2g}^6e_g^1$) is more favorable toward ORR/OER catalytic activity. Furthermore, the generated V_o enhanced the formation and further decomposition of Li_2O_2 and hampered side reactions between the cathode and electrolyte (Fig. 6(j)). As a result, the LOB using the LNO cathode reached a high discharge capacity of up to 5910 mA h $g_{cathode}^{-1}$ at 50 mA $g_{cathode}^{-1}$. Though anion dopants in the O-site have been investigated in semiconductors to adjust the bandgap energy, few studies of anion-doped perovskites as catalysts for LOBs have been reported.

4.3 Oxygen vacancy

The role of oxygen defects in perovskites cannot be neglected because they can tune the electronic structure, surface chemistry and crystalline nanostructures, thereby modifying the physicochemical properties of catalysts.[111]

The creation of V_o modulates the interaction between the B-site TM and oxygen molecules. The e_g-filling of the B-site cation is a decisive factor in determining oxygen adsorption/desorption energy. A lower e_g-filling results in strong B–O_2 bonds, and a higher e_g-filling contributes to weak bonding.[45] As well as the cation doping discussed above, annealing materials under a reducing atmosphere is another viable approach to create V_o in perovskites. For example, V_o was introduced to $CaMnO_3$ through thermal treatment under mixed H_2/Ar gas at 300 °C. The presence of V_o in $CaMnO_3$ created mixed-valence Mn^{3+}/Mn^{4+} states, modifying the electronic structure of $CaMnO_3$.[45] The mixed Mn^{4+} ($t_2g^3e_g^0$) and Mn^{3+} ($t_{2g}^3e_g^1$) exhibited an intermediate e_g occupation,

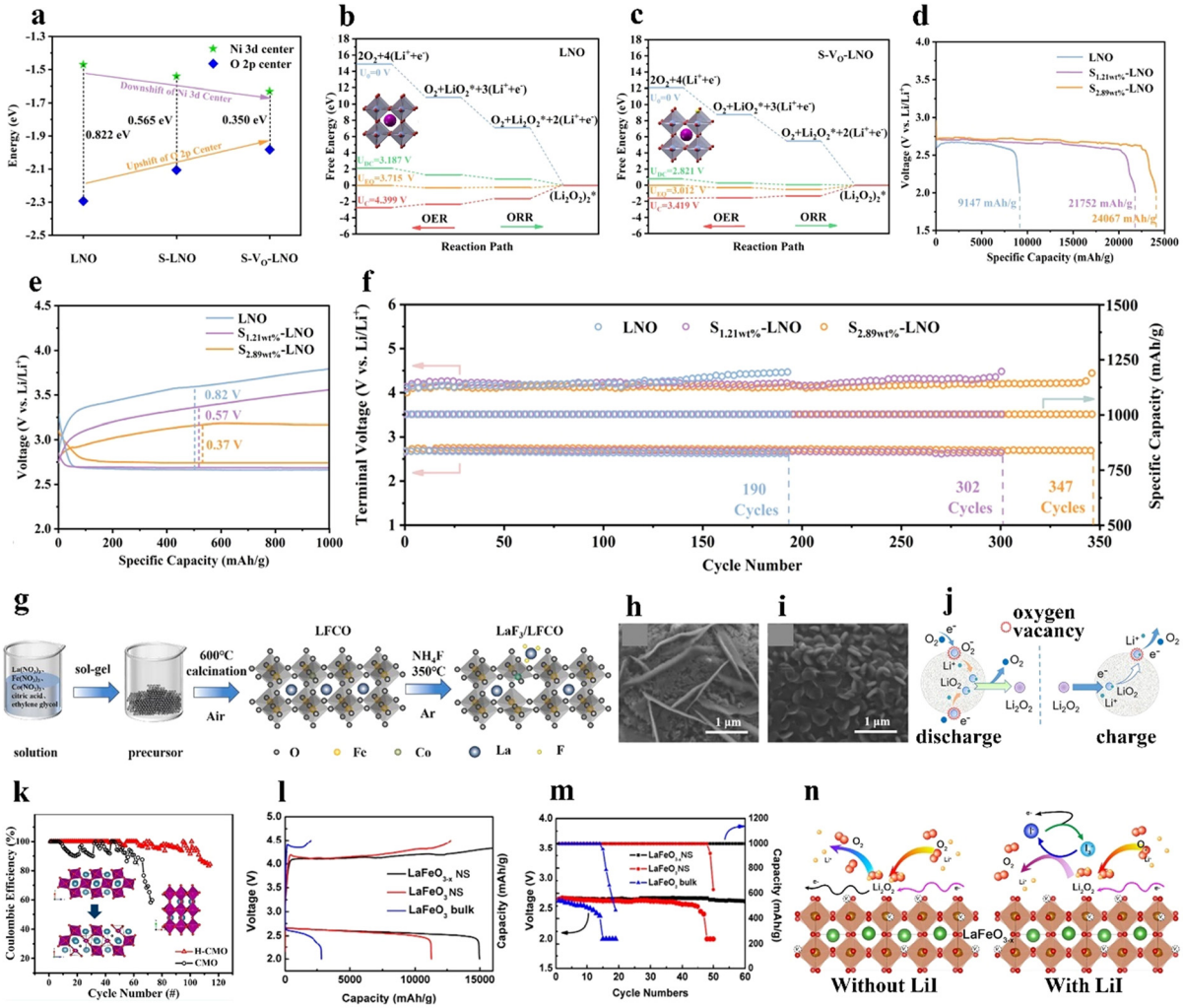

Fig. 6 The impact of B-site substitution and oxygen vacancies on perovskites. (a) Illustration of Ni 3d and O 2p band centers S-V_o-LNO and control samples. Free energy diagram of the ORR on (b) LNO and (c) S-V_o-LNO. (d) Discharge curves at 100 mA g^{-1}, (e) discharge/charge curves with a confined capacity of 1000 mA h g^{-1} at 100 mA g^{-1}. (f) Cycling stability of the LOBs with LNO and S-V_o-LNO cathodes. (a)–(f) Reproduced with permission.[68] Copyright 2022, Elsevier. (g) Illustration of the synthesis process of LaF_3/LFCO. SEM images of (h) LFCO and (i) LaF_3/LFCO cathodes after the first discharge. (g)–(i) Reproduced with permission.[69] Copyright 2022, Elsevier. (j) Formation and decomposition processes of Li_2O_2 on N-doped LNO during the discharge/charge process. Reproduced with permission.[70] Copyright 2018, American Chemical Society. (k) Coulombic efficiency of H-CMO and CMO. Insets: Their crystal structures. Reproduced with permission.[45] Copyright 2020, American Chemical Society. (l) The initial capacity at 100 mA g^{-1} and (m) cycling stability of $LaFeO_3$ and $LaFeO_{3-x}$. (n) ORR and OER mechanisms on the $LaFeO_{3-x}$ surface with/without LiI. (k)–(n) Reproduced with permission.[76] Copyright 2020, Elsevier.

facilitating the formation of superoxide and Li_2O_2 and resulting in better ORR activity (a smaller Tafel slope of -0.756 V dec^{-1}). Multiple valences of the B-site cation and unique structural arrangements, along with the good ionic conductivity of perovskite oxides, collectively promote the $B^{(n+1)+}/B^{n+}$ redox reaction. Accordingly, the LOB using defective $CaMnO_3$ (H-CMO) provided an improved cycling capability of 114 cycles with a limited capacity of 500 mA h g^{-1} at 500 mA g^{-1} (Fig. 6(k)). The LOB using H-CMO achieved a higher capacity of around 3600 mA h g^{-1} at 250 mA g^{-1}, outperforming the cell using CMO (2750 mA h g^{-1}).

The presence of V_o in perovskites optimizes the surface adsorption energy, provides a large body of active sites and promotes Li^+ or e^- conductivity. Gao *et al.*[76] produced V_o in $LaFeO_{3-x}$ by calcination of the pristine $LaFeO_3$ under Ar gas, which distorted the FeO_6 octahedra and changed the valence state of Fe. Theoretical calculation results suggested that O_2 molecules tended to adsorb on the surface-defective sample more than on $LaFeO_3$. The existence of Fe with different valence states can increase ionic and electronic conductivity. Accordingly, the LOB with oxygen-defective $LaFeO_{3-\sigma}$ showed a higher initial capacity, better rate capacity, and longer cycle life than that with $LaFeO_3$ (Fig. 6(l) and (m)). Moreover, an LiI redox mediator was used to further reduce the overpotential due to the I_3^- to I^- redox reaction (Fig. 6(n)). However, the lack of accurate control of the V_o content continues to hamper efforts to quantitatively investigate the structure–activity relationship between V_o and catalytic activity.

4.4 Perovskite-based composite catalysts

Combining perovskite oxides with conductive substances such as carbon, MOFs, MXene, and metal compounds is a feasible way to enhance their electrochemical activity and overcome their intrinsic low conductivity. The intimate interfacial interplay between dual materials gives rise to unique electronic structures and improved structural stability.

Perovskite/carbon composites. Porous carbon materials such as 3D graphene with favorable electrical conductivity, high surface area, and controllable porosity have been used as suitable substrates to load with perovskite oxides, as they not only maximize the utilization of active sites but also facilitate the infiltration of electrolyte.[26,31,74,76,77,94,112,113] A dip-coating method was used to prepare carbon/perovskite composites, in which the carbon substrate is immersed in a precursor solution and surfactant, followed by the hydrolysis and condensation of the precursor.[113] Kim *et al.*[31] hybridized $Nd_{1.5}Ba_{1.5}CoFeMnO_{9-\delta}$ with N-doped rGO to produce a highly active bifunctional ORR/OER catalyst, which exhibited efficient charge transfer, oxygen-defective structure, and small hybridization strength between Co 3d and O 2p orbitals.

In addition, carbon nanofibers or nanosheets have been adopted as ideal frameworks to load with perovskites as conductive and highly porous free-standing cathodes.[74,113,114] Yang *et al.*[113] prepared sandwich-like graphene/mesoporous LaSrMnO nanosheets as free-standing cathodes for LOBs. Mesopores offered a high surface area for loading discharged products and easy access channels for the electrolyte, and served as reservoirs of O_2 to feed the ORR/OER reactions. Macropores between nanosheets expedited Li^+ diffusion and O_2 transport into the inner space of the catalyst. In the composite, the perovskite phase was responsible for decreasing the reaction overpotential, and the graphene foam acted as a conductive medium to promote electron transport, provided sufficient room for the deposition/decomposition of Li_2O_2 and prevented the clogging of the discharged resultants. Accordingly, the assembled LOB demonstrated a high specific capacity, rate capability, and long cycling life.

Unfortunately, the electrochemical oxidation of carbon materials under high potentials during the OER process deactivates active sites. Highly active oxygen radicals like O^{2-}, LiO_2 and Li_2O_2 corrode carbon materials, and decompose carbons and organic electrolytes, shortening the cycle life of LOBs.[84] Highly durable frameworks for loading perovskite oxides are thus required.

Perovskite/MOF composite. MOFs with well-defined pore structures can act as suitable scaffolds to load perovskite nanoparticles. Their adjustable pore configurations can match the geometry and size of perovskite nanocrystals and guarantee easy accessibility for reagents during synthesis. Qiao[92] confined $CsPbBr_3$ nanocrystals into a mesoporous Fe-MOF (4.2 and 5.5 nm) to derive a perovskite/MOF hybrid catalyst ($CsPbBr_3$@PCN-333(Fe)) by a sequential deposition method, where perovskite nanocrystals were stabilized from leaching or aggregation due to the confinement effect of the MOF cages. As shown in Fig. 7(a)–(c), the electrons of $CsPbBr_3$ could be completely transferred to the MOF when they were in the cage, while only a fraction of the electrons were transferred to the external interface. No electron transfer happened if $CsPbBr_3$ was far away from the MOF. Interestingly, the O_2/Li_2O_2 redox couple resided between the valence band (VB) and conduction band (CB) of $CsPbBr_3$ and the MOF (Fig. 7(d)). Photoelectrons and holes in the composite can be excited and then transported to the CB and VB under irradiation, conducive for the use of solar energy. The LOB with a $CsPbBr_3$@PCN-333(Fe) photocathode demonstrated a high discharge voltage of 3.19 V with a round-trip efficiency of 92.7% and could be stably cycled for above 200 h at 0.01 mA cm^{-2} under illumination.

Perovskite/noble metal composites. Bifunctional catalysts have been prepared by combining perovskite oxides with novel metal nanoparticles or TM compounds, such as Pd and Ag nanoparticles, RuO_2, CoO, Co_3O_4, Fe_2O_3, and Ni_3S_2.[25,38,59,73,78–81] Carbon-free catalysts avoid the decomposition of carbon by highly oxidative radicals. Owing to its high catalytic activity and superior electrical conductivity ($\sim 10^4$ S cm^{-1}), RuO_2 has been combined with perovskites to enhance electron-transfer kinetics at the interface between the cathode and oxygen intermediates.[73,115,116] The LiOH reaction product is derived from the reaction between Li_2O_2 and H_2O, and Li_2CO_3 comes from electrolyte decomposition and the reaction product of carbon and Li_2O_2.[73] Therefore, designing electrocatalysts that can decompose both LiOH and Li_2CO_3 is an effective way to boost the performance of LOBs. Sun *et al.*[73] used a wet impregnation method to grow RuO_2 nanoparticles on a 1D porous $La_{0.6}Sr_{0.4}Co_{0.8}Mn_{0.2}O_3$ nanofiber (LSCM NF). Owing to their good electrical conductivity and superior OER/ORR catalytic performance, RuO_2 was capable of decomposing LiOH and Li_2O_2, and the LSCM NFs could decompose the reaction side-product of Li_2CO_3. The composite electrode had a large initial capacity of 12 742 mA h g^{-1} at 50 mA g^{-1}, a low voltage range of 2.6–4.3 V, and a stable cycle life ($\geq$100 cycles with a limited capacity of 500 mA h g^{-1} at 50 mA g^{-1}), as shown in Fig. 7(e).

Interestingly, water vapor as an additive was introduced to oxygen gas in the solid-state LOB, which transformed the discharge product from growth-limited Li_2O_2 to easily formed LiOH, and improved the specific capacity of the LOB.[38,117] Kim *et al.*[38] hybridized electron conducting RuO_2 and $La_2LiRuO_{6-\delta}$ as a highly active electrocatalyst for a LiOH-related reaction in a solid-state LOB to increase capacity and cycle life (665 cycles with a limited capacity of 200 mA h $g_{cathode}^{-1}$ at 100 mA $g_{cathode}^{-1}$) (Fig. 7(f)). Humidity increased the discharge voltage of the LOB to 3.4 V, surpassing the cell operated under dry oxygen (2.96 V) (Fig. 7(g) and (h)). LiOH was capable of absorbing water vapor and became hydrated LiOH as a Li^+-ion conductor, boosting the reaction kinetics.

Furthermore, due to its cheap price, good conductivity, and catalytic activity, metallic Ag has also been combined with perovskites as a cathode for LOBs.[87,118] Zou *et al.*[118] took advantage of the heterostructural interface between the conductive Ag nanoparticles and a $PrBa_{0.5}Sr_{0.5}Co_2O_{5+\delta}$ (PBSC)

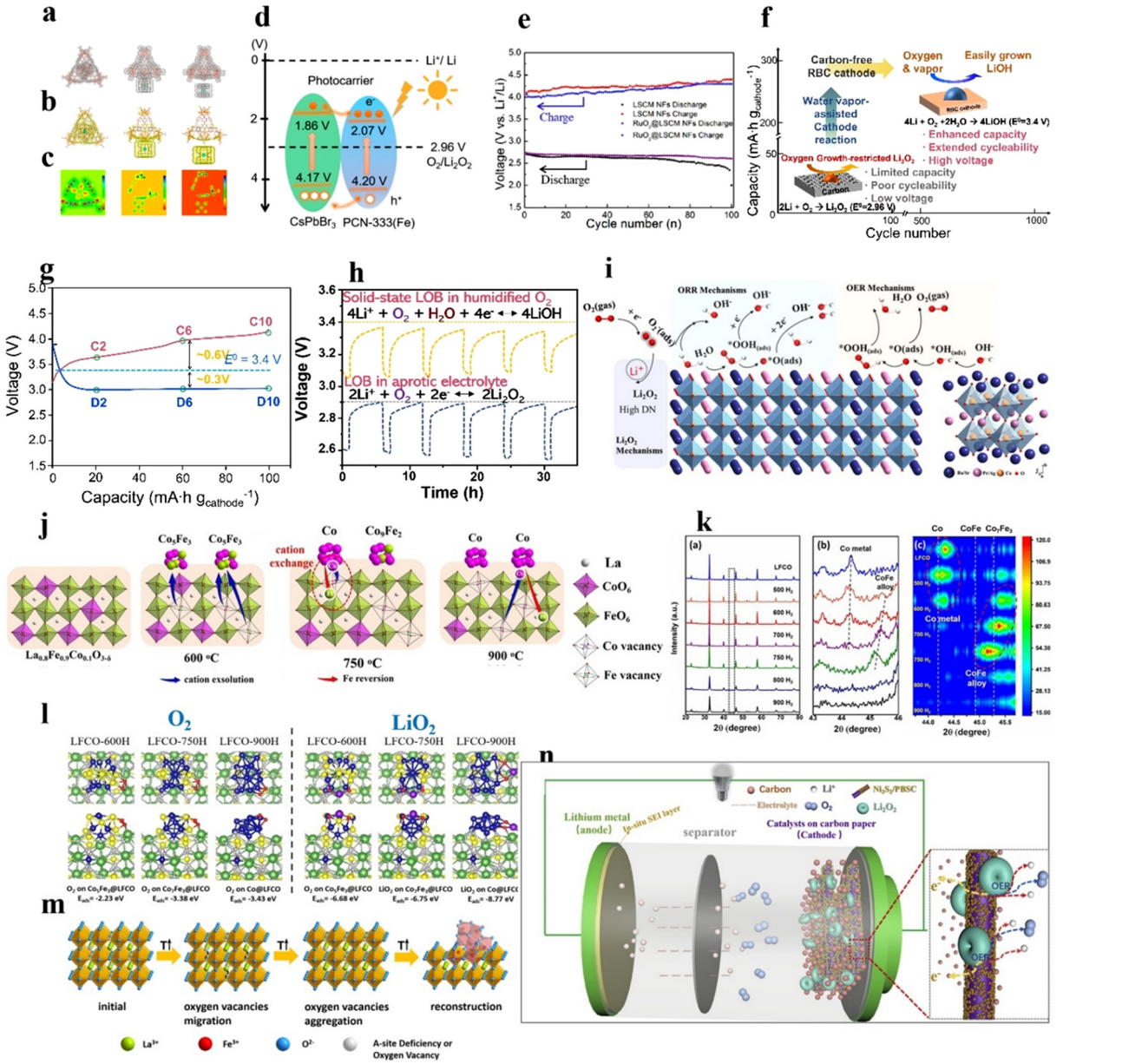

Fig. 7 Perovskite-based composite catalysts. (a) Charge density of $CsPbBr_3$ inside the cage, outside the cage, and isolated. (b) Corresponding charge density difference. (c) Corresponding 2D deformation charge density. (d) Demonstration of the VB and CB energy levels and the redistribution of photocarriers between PCN-333(Fe) and $CsPbBr_3$ under light. (a)–(d) Reproduced with permission.[92] Copyright 2021, American Chemical Society. (e) Discharge/charge terminal voltages of LOBs with RuO_2@LSCM NF and LSCM NF cathodes. Reproduced with permission.[73] Copyright 2021, American Chemical Society. (f) Schematic illustration of a solid-state LOB. (g) Discharge–charge curves of LOBs in humidified O_2. (h) Galvanostatic intermittent titration technique (GITT) results of the LOB tested in liquid electrolyte without water vapor. (i) Schematic illustration of the ORR/OER at the Ag/PBSC heterostructure surface. Reproduced with permission.[118] Copyright 2022, Wiley-VCH. (j) Dual-exsolution of LFCO controlled by temperature. (k) XRD patterns, enlarged XRD pattern at 43–46°, and depth view of the XRD pattern at 43.4–45.8° of LFCO. (l) Binding energy of O_2 and LiO_2 on LFCO obtained at different temperatures. (j)–(l) Reproduced with permission.[81] Copyright 2022, Wiley-VCH. (m) Schematic illustration of the preparation of the α-Fe_2O_3/$LaFeO_{3-x}$ composite. Reproduced with permission.[90] Copyright 2018, American Chemical Society. (n) Schematic illustration of the LOB employing Ni_3S_2/PBSC cathodes, and schematic of the charging process. Reproduced with permission.[78] Copyright 2019, Elsevier.

perovskite, and demonstrated that Ag could nucleate Li_2O_2 with a low overpotential (Fig. 7(i)).

Perovskite/TM composites. The crystallinity and morphology of Li_2O_2 impacts the electrochemical performance of LOBs. Large-sized Li_2O_2 generally results in a high specific capacity and durable cycling longevity, while a film-like amorphous discharge product contributes to fast ion and electron transport, exhibiting an easier decomposition process during charging.[24] The metal component and perovskite can synergistically optimize the binding strength with O_2 and LiO_2, which modulates the discharge reaction pathways. Cong *et al.*[81] prepared a CoFe alloy and Co-metal-decorated $La_{0.8}Fe_{0.9}Co_{0.1}O_{3-\delta}$

(LFCO) catalyst by annealing the pristine perovskite under 5% H_2/Ar atmosphere. With the increased annealing temperature, nanoparticles indexed to the CoFe alloy and Co metal gradually appeared on the surface of the perovskites, as indicated by X-ray diffraction (XRD) results (Fig. 7(j) and (k)). At 600 °C, Co and Fe species exsolved from the parent perovskite to generate an alloy at the surface to form LFCO-600H, while the Fe component in the alloy started to exchange with Co at 750 °C. At 900 °C, the increased Co species finally became a metallic state. DFT calculation results (Fig. 7(l)) indicated that due to the weak adsorption between the CoFe alloy, O_2 and LiO_2, lithium superoxide was generated at the LFCO-600H surface by a one-electron reduction step and diffused to the electrolyte. It transformed to Li_2O_2 and O_2 *via* a disproportionation reaction, generating ring-like Li_2O_2. However, the strong binding strength of Co metal in LFCO-900H with O_2/LiO_2 led to the formation of thin-film-like Li_2O_2. Due to the interaction between the CoFe alloy/Co metal and the parent perovskite, as well as a high degree of structural distortion, LFCO-750H demonstrated moderate binding strength. Accordingly, the LOB using the LFCO-750 cathode exhibited a high discharge capacity of 6549.7 mA h g^{-1} at 100 mA g^{-1} and negligible capacity fading after 215 cycles compared to LFCO-600 and LFCO-900, the samples annealed at 600 °C and 900 °C.

The segregation of TM oxides in A-site defective perovskites can promote LOB performance. For example, the formation of V_o during the thermal treatment of $La_{0.85}FeO_{3-\delta}$ at 900 °C resulted in the segregation of α-Fe_2O_3 (Fig. 7(m)).[90] In the composite, the interaction between $LaFeO_{3-x}$ and α-Fe_2O_3 led to structural distortion, exposing ample active sites for the OER/ORR. The LOB with the composite catalyst exhibited a longer cycle life (108 cycles) than that with α-Fe_2O_3 (21 cycles) and $La_{0.85}FeO_{3-\delta}$ (51 cycles) catalysts. In another example, Ni nanoparticles were exsolved on the $La_{0.9}Mn_{0.6}Ni_{0.4}O_{3-\delta}$ nanofiber surface during thermal treatment under a H_2/Ar atmosphere.[88] The interaction between metal nanoparticles and perovskite and the formation of V_o synergistically increased the number of active sites, and improved electrical conductivity and O_2 adsorption.

Ni, Co, and Fe-based compounds with favorable catalytic activity have been combined with perovskites to prepare hybrid catalysts with the collective superiorities of dual-functional materials. Zhang *et al.*[78] used an atomic-layer-deposition approach to deposit a layer of Ni_3S_2 (10 nm) on 1D $PrBa_{0.5}Sr_{0.5}Co_2O_{5+\delta}$ (PBSC) nanofibers as an integrated catalyst. The Li_2O_2 discharge product could be effectively decomposed to Li^+ and O_2 by virtue of the high OER activity of the PBSC and Ni_3S_2. The peroxide combined with V_o in the PBSC and then oxidized to oxygen, and the nanosized Ni_3S_2 and unique 1D porous PBSC could rapidly transfer electrons from active sites to the current collector. The assembled LOB (Fig. 7(n)) showed a low overpotential of 0.68 V at 1000 mA h g^{-1}), large capacity (12 874 mA h g^{-1} at 100 mA g^{-1}), and long cycle life (>120 cycles with a limited capacity of 1000 mA h g^{-1} at 100 mA g^{-1}). Another example shows that FeOOH clusters on the $LaNiO_3$ surface enhanced OH^- adsorption and weakened the Ni–O bond in an alkaline electrolyte, which optimized the OH^- filling barrier to boost the lattice O-involved OER and decreased the reaction barrier of the LOM.[59] Co_3O_4 nanoparticles on $LaCo_{0.6}Ni_{0.4}O_3$ facilitated O_2 adsorption on the catalyst surface and O_2/Li_2O_2 conversion.[119] In addition to the above-mentioned materials, $Ti_3C_2T_x$ nanosheets with low Li ionic diffusion barriers (<0.07 eV) have been used as substrates to load $La_{0.5}Sr_{0.5}CoO_{3-\delta}$ perovskite as a catalyst for LOBs.[27] The derived LOB could be operated over 80 cycles at 500 mA g^{-1} with a restriction of 1000 mA h g^{-1}, superior performance to that of $La_{0.5}Sr_{0.5}CoO_{3-\delta}$ (15 cycles) and $Ti_3C_2T_x$ (9 cycles).

5. Conclusion

Perovskite oxides have been studied as promising ORR/OER electrocatalysts due to their favorable catalytic activity, tunable compositions and nanostructures. This mini-review analyzes the recent advances in perovskite oxide electrocatalysts for LOBs, and highlights the synthetic techniques, fundamental catalytic mechanisms, and various strategies for the enhancement of catalytic performance. There is ample space to advance this technology by exploring the ORR/OER mechanisms, porous structure development, composition regulation, defect engineering, and composite synthesis for perovskite oxides in nonaqueous LOBs. Below is a summary of the existing challenges in the use of perovskite oxides as catalysts.

(i) Notwithstanding massive endeavors to study the catalytic mechanisms of perovskite oxides for the ORR/OER in aqueous electrolytes, the investigation of fundamental catalytic mechanisms in the nonaqueous electrolyte scenario is still in its infancy. The relationship between the composition, crystal structure, and catalytic performance needs to be clarified and deeply investigated, as this knowledge is critical for guiding the design of highly active catalysts for LOBs.

It should be noted that in aqueous alkaline electrolytes, *in situ* surface reconstruction or amorphization of perovskites could occur by anodic polarization during the OER, which has been proved to be beneficial for enhancing the OER performance.[120–122] A-site cations have high solubility in alkaline electrolytes, and BO_2 metal oxides also suffer from chemical dissolution during the lattice-involved OER process. The dissolved B-site cations either release to the bulk electrolyte or react with OH^- ions and then deposit on the material surface to form an oxyhydroxide phase.[123] The processes can be described in eqn (8)–(11):

$$2ABO_3 \leftrightarrow 2BO_2 + 2A^{2+} + O_2 + 4e^- \quad (8)$$

$$2ABO_3 + 2H_2O \leftrightarrow 2BO_2 + 2A^{2+} + 4KOH \quad (9)$$

$$BO_2 \leftrightarrow O_2 + B^{4+} + 4e^- \quad (10)$$

$$BO_2 + 2H_2O \leftrightarrow B^{4+} + 4OH^- \quad (11)$$

Of particular note, the surface reconstruction of perovskites in nonaqueous electrolytes has rarely been studied. It is speculated that it could occur when the surface lattice oxygen

participates in the catalytic process. More explicitly, the active lattice oxygen of perovskites can assist in adsorbing Li^+ ions from the aprotic electrolyte due to its shallower O 2p band adjacent to the Fermi level to donate electrons.[61] After that, the generated electrophilic oxyl groups on the surface serve as initial growth species to react with nucleophilic moieties like LiO_2, triggering the formation of the discharge product.[17,61] Even though the surface lattice oxygen as catalytic sites has been proved to improve the ORR/OER kinetics, it may give rise to the generation of surface oxygen defects. Oxygen defects will be compensated by generating cationic vacancies, leading to the dissolution of surface cations and eventually resulting in the instability of the catalyst surface.[61,124] As a result, the surface composition and nanostructure of perovskites are altered due to the formation of oxygen defects and the dissolution of surface cations. In this regard, the change in the surface electronic structure, crystallinity, valence state, and coordination environment of cations, and morphology of perovskite oxides upon cycling can be investigated by *in situ* or *ex situ* characterizations such as *in situ* TEM, Raman, X-ray absorption spectroscopy, *etc.* These techniques help to understand how these changes influence the catalytic activity and durability of cathodes for LOB. The combination of results from advanced characterization, experiments, and theoretical calculations is required for a comprehensive understanding of the underlying mechanisms of the reaction occurring at specific active sites under operando status.

(ii) Myriad cations or anions can be accommodated at the A-, B-, and O-sites of perovskites, ensuring the versatile adjustment of their properties for optimized catalytic performance. Screening and synthesis of ideal perovskite oxide catalysts are challenging and tedious processes due to the multitude of choices of elements. Therefore, artificial intelligence such as machine learning and high-throughput calculations can be used to gain unique insights and to screen highly active catalysts based on data sets. This will enable researchers to design materials with optimized compositions and ideal experimental parameters.[29,125,126]

(iii) High specific surface areas and controllable porosities are required to provide ample catalytically active spots and allow easy transport of reactants. It is known that the large-area triple boundaries, where oxygen, electrolyte, and oxygen cathodes exist, play crucial roles in effectively transporting mass and accommodating the discharged products. However, perovskite oxide catalysts prepared by the current synthetic methods (*e.g.*, sol–gel and solid-state reaction) show a small SSA (<300 m^2 g^{-1}), uncontrollable pore structures, and irregular morphology in some cases, impeding mass transport. Novel 3D-printed ordered perovskite,[127] self-assembled anti-perovskites,[128] and 3D structured perovskitoids[39] with large SSAs, controllable morphologies and tailorable porous architectures may overcome these challenges, and are promising cathode candidates for LOBs.

(iv) It is imperative to pay attention to the activity-stability tradeoff of perovskites. Long cycling stability of energy-storage devices is a prerequisite for real-world applications, while LOBs with perovskite cathodes can be operated for only several hundred cycles (<200 cycles in many cases), which is unfavorable for practical applications. The poor cycling stability of LOB batteries with perovskite cathodes can be attributed to the following reasons. First, the insoluble Li_2O_2 product covered on the perovskite surface blocks oxygen diffusion pathways, leading to severe volume expansion of the air cathode, and inducing side reactions at the cathode.[20] Due to limited active sites at the Li_2O_2/catalyst interface, voltage polarization could occur and the reaction kinetics for the ORR/OER become sluggish.[20] Second, metal elements in perovskites facilitate the generation of metal–O bonds in an O_2-rich environment, which may gradually degrade the material structure. Third, some perovskites can be partially decomposed in aprotic solvents. For example, due to the reaction between positive Pb^{2+} ions and polar aprotic solvents, the PbI_6 octahedral framework collapsed in a trihalide perovskite.[129] Moreover, the improved catalytic activity of surface lattice oxygen of perovskites is at the expense of surface stability, where surface cations will be dissolved in the electrolyte, and bulk cation ions migrate to the surface area, resulting in instability of perovskite structures. To circumvent these obstacles, a porous structure of the cathode is highly required to increase oxygen diffusion paths and the number of nucleation sites for the discharged product, effectively decreasing the overpotential during charging/discharging processes of LOBs. Furthermore, soluble redox mediators could be introduced to the electrolyte to tune the formation and decomposition pathways of Li_2O_2 for further decreasing the overpotential of the ORR and OER. On top of that, nanostructured perovskite oxides (nanocrystals or quantum dots) can be combined with large-surface-area materials, such as graphene, porous carbon, MOFs, and covalent organic frameworks to harness the collaborative benefits of multiple active components. Meanwhile, a high loading of perovskite oxide on the substrates is required to achieve high catalytic performance.

Conflicts of interest

The authors declare no competing interests.

Acknowledgements

This research was supported by Creative Materials Discovery Program through the National Research Foundation of Korea (NRF) funded by Ministry of Science and ICT (NRF-2020M3D1A1110522 and NRF-2022R1A2B5B03001781).

References

1 J. L. Holechek, H. M. E. Geli, M. N. Sawalhah and R. Valdez, *Sustainability*, 2022, **14**, 4792.
2 R. Zhang, H. Zhou, P. Sun, Q. Ma, M. Lu, H. Su, W. Yang and Q. Xu, *Battery Energy*, 2022, **1**, 20220023.

3 C. Y. J. Lim and Z. W. Seh, *Battery Energy*, 2022, **1**, 20220008.
4 Y. Guo, Y. Zhang and H. Lu, *Battery Energy*, 2022, **1**, 20210014.
5 C. Shu, J. Wang, J. Long, H. K. Liu and S. X. Dou, *Adv. Mater.*, 2019, **31**, 1804587.
6 M. D. Radin and D. J. Siegel, *Energy Environ. Sci.*, 2013, **6**, 2370–2379.
7 T. Liu, J. P. Vivek, E. W. Zhao, J. Lei, N. Garcia-Araez and C. P. Grey, *Chem. Rev.*, 2020, **120**, 6558–6625.
8 W. J. Kwak, R. Sharma, D. Sharon, C. Xia, H. Kim, L. R. Johnson, P. G. Bruce, L. F. Nazar, Y. K. Sun, A. A. Frimer, M. Noked, S. A. Freunberger and D. Aurbach, *Chem. Rev.*, 2020, **120**, 6626–6683.
9 K. Yoo, S. Banerjee, J. Kim and P. Dutta, *Energies*, 2017, **10**, 1748.
10 M. Park, C. Liang, T. H. Lee, D. A. Agyeman, J. Yang, V. W. Hei Lau, S. Il Choi, H. W. Jang, K. Cho and Y. M. Kang, *Adv. Energy Mater.*, 2020, **10**, 1903225.
11 Y. K. Jo, W. Tamakloe, X. Jin, J. Lim, S. B. Patil, Y. M. Kang and S. J. Hwang, *Appl. Catal., B*, 2019, **254**, 523–530.
12 Y. Bae, H. Park, Y. Ko, H. Kim, S. K. Park and K. Kang, *Batteries Supercaps*, 2019, **2**, 311–325.
13 T. H. Gu, D. A. Agyeman, S. J. Shin, X. Jin, J. M. Lee, H. Kim, Y. M. Kang and S. J. Hwang, *Angew. Chem., Int. Ed.*, 2018, **130**, 16216–16221.
14 K. Song, J. Jung, M. Park, H. Park, H. J. Kim, S. Il Choi, J. Yang, K. Kang, Y. K. Han and Y. M. Kang, *ACS Catal.*, 2018, **8**, 9006–9015.
15 D. A. Agyeman, M. Park and Y. M. Kang, *J. Mater. Chem. A*, 2017, **5**, 22234–22241.
16 K. Song, E. Cho and Y. M. Kang, *ACS Catal.*, 2015, **5**, 5116–5122.
17 Y. Zheng, K. Song, J. Jung, C. Li, Y. U. Heo, M. S. Park, M. Cho, Y. M. Kang and K. Cho, *Chem. Mater.*, 2015, **27**, 3243–3249.
18 D. A. Agyeman, K. Song, S. H. Kang, M. R. Jo, E. Cho and Y. M. Kang, *J. Mater. Chem. A*, 2015, **3**, 22557–22563.
19 H. Song, R. Choi, J. Jung, G. Kim, K. Song, Y. Il Kim, S. C. Jung, Y. K. Han and Y. M. Kang, *Energy Environ. Sci.*, 2014, **7**, 1362–1368.
20 Z. Chang, J. Xu and X. Zhang, *Adv. Energy Mater.*, 2017, **7**, 1700875.
21 W. Bai, Z. Zhang, K. Wang and J. Chen, *Battery Energy*, 2022, **1**, 20220019.
22 Y. Lai, Y. Jiao, J. Song, K. Zhang, J. Li and Z. Zhang, *Mater. Chem. Front.*, 2018, **2**, 376–384.
23 Y. Yang, X. Xue, Y. Qin, X. Wang, M. Yao, Z. Qin and H. Huang, *J. Phys. Chem. C*, 2018, **122**, 12665–12672.
24 Y. Liu, J. Cai, J. Zhou, Y. Zang, X. Zheng, Z. Zhu, B. Liu, G. Wang and Y. Qian, *eScience*, 2022, **2**, 389–398.
25 J. Wang, X. Cheng, Z. Li, M. Xu, Y. Lu, S. Liu, Y. Zhang and C. Sun, *ACS Appl. Energy Mater.*, 2018, **1**, 5557–5566.
26 J. Cheng, Y. Jiang, M. Zhang, L. Zou, Y. Huang, Z. Wang, B. Chi, J. Pu and J. Li, *Phys. Chem. Chem. Phys.*, 2017, **19**, 10227–10230.
27 Z. Sun, M. Yuan, L. Lin, H. Yang, C. Nan, G. Sun, H. Li and X. Yang, *ACS Appl. Energy Mater.*, 2019, **2**, 4144–4150.
28 W. Xiong, H. Yin, T. Wu and H. Li, *Eur. J. Chem.*, 2022, **29**, e202202872.
29 J. Hwang, R. R. Rao, L. Giordano, Y. Katayama, Y. Yu and Y. Shao-Horn, *Science*, 2017, **358**, 751–756.
30 Q. Ji, L. Bi, J. Zhang, H. Cao and X. S. Zhao, *Energy Environ. Sci.*, 2020, **13**, 1408–1428.
31 N. I. Kim, Y. J. Sa, T. S. Yoo, S. R. Choi, R. A. Afzal, T. Choi, Y. S. Seo, K. S. Lee, J. Y. Hwang, W. S. Choi, S. H. Joo and J. Y. Park, *Sci. Adv.*, 2018, **4**, eaap9360.
32 J. Suntivich, K. J. May, H. A. Gasteiger, J. B. Goodenough, Y. Shao-horn, F. Calle-vallejo, A. D. Oscar, M. J. Kolb, M. T. M. Koper, J. Suntivich, K. J. May, H. A. Gasteiger, J. B. Goodenough and Y. Shao-horn, *Science*, 2011, **334**, 1383–1385.
33 J. Suntivich, H. A. Gasteiger, N. Yabuuchi, H. Nakanishi, J. B. Goodenough and Y. Shao-Horn, *Nat. Chem.*, 2011, **3**, 546–550.
34 M. A. Peña and J. L. G. Fierro, *Chem. Rev.*, 2001, **101**, 1981–2017.
35 J. X. Flores-Lasluisa, F. Huerta, D. Cazorla-Amorós and E. Morallón, *Environ. Res.*, 2022, **214**, 113731.
36 K.-L. Wang, Y.-G. Yang, Y.-H. Lou, M. Li, F. Igbari, J.-J. Cao, J. Chen, W.-F. Yang, C. Dong, L. Li, R.-Z. Tai and Z.-K. Wang, *eScience*, 2021, **1**, 53–59.
37 X. Li, W. Ma, D. Liang, W. Cai, S. Zhao and Z. Zang, *eScience*, 2022, **2**, 646–654.
38 M. Kim, H. Lee, H. J. Kwon, S. Bak, C. Jaye, D. A. Fischer, G. Yoon, J. O. Park, D. Seo, S. B. Ma and D. Im, *Sci. Adv.*, 2022, **2**, eabm8584.
39 Y. Miao, X. Wang, H. Zhang, T. Zhang, N. Wei, X. Liu, Y. Chen, J. Chen and Y. Zhao, *eScience*, 2021, **1**, 91–97.
40 S. Zhou, X. Miao, X. Zhao, C. Ma, Y. Qiu, Z. Hu, J. Zhao, L. Shi and J. Zeng, *Nat. Commun.*, 2016, **7**, 11510.
41 B. Zhao, L. Zhang, D. Zhen, S. Yoo, Y. Ding, D. Chen, Y. Chen, Q. Zhang, B. Doyle, X. Xiong and M. Liu, *Nat. Commun.*, 2017, **8**, 14586.
42 M. Sung, G. Lee and D. Kim, *InfoMat*, 2021, **3**, 1295–1310.
43 D. Du, R. Zheng, X. Chen, W. Xiang, C. Zhao, B. Zhou, R. Li, H. Xu and C. Shu, *ACS Appl. Mater. Interfaces*, 2021, **13**, 33133–33146.
44 X. Liu, H. Gong, T. Wang, H. Guo, L. Song, W. Xia, B. Gao, Z. Jiang, L. Feng and J. He, *Chem. – Asian J.*, 2018, **13**, 528–535.
45 G. S. Hegde, A. Ghosh, R. Badam, N. Matsumi and R. Sundara, *ACS Appl. Energy Mater.*, 2020, **3**, 1338–1348.
46 H. Wang, M. Zhou, P. Choudhury and H. Luo, *Appl. Mater. Today*, 2019, **16**, 56–71.
47 K. Wang, C. Han, Z. Shao, J. Qiu, S. Wang and S. Liu, *Adv. Funct. Mater.*, 2021, **31**, 2102089.
48 M. Zhang, G. Jeerh, P. Zou, R. Lan, M. Wang, H. Wang and S. Tao, *Mater. Today*, 2021, **49**, 351–377.
49 D. Aurbach, B. D. McCloskey, L. F. Nazar and P. G. Bruce, *Nat. Energy*, 2016, **1**, 16128.
50 R. Jacobs, J. Hwang, Y. Shao-Horn and D. Morgan, *Chem. Mater.*, 2019, **31**, 785–797.

51 H. Lee, O. Gwon, K. Choi, L. Zhang, J. Zhou, J. Park, J. W. Yoo, J. Q. Wang, J. H. Lee and G. Kim, *ACS Catal.*, 2020, **10**, 4664–4670.
52 X. Wu, W. Yu, K. Wen, H. Wang, X. Wang, C. W. Nan and L. Li, *J. Energy Chem.*, 2021, **60**, 135–149.
53 A. Khetan, A. Luntz and V. Viswanathan, *J. Phys. Chem. Lett.*, 2015, **6**, 1254–1259.
54 Y. Zhou, Y. Zhao, Z. Liu, Z. Peng, L. Wang and W. Chen, *J. Energy Chem.*, 2021, **55**, 55–61.
55 X. Gao, Y. Chen, L. Johnson and P. G. Bruce, *Nat. Mater.*, 2016, **15**, 882–888.
56 Q. Li, J. Wu, T. Wu, H. Jin, N. Zhang, J. Li, W. Liang, M. Liu, L. Huang and J. Zhou, *Adv. Funct. Mater.*, 2021, **31**, 2102002.
57 Y. Zhu, W. Zhou, Z. G. Chen, Y. Chen, C. Su, M. O. Tadé and Z. Shao, *Angew. Chem., Int. Ed.*, 2015, **54**, 3897–3901.
58 S. Yagi, I. Yamada, H. Tsukasaki, A. Seno, M. Murakami, H. Fujii, H. Chen, N. Umezawa, H. Abe, N. Nishiyama and S. Mori, *Nat. Commun.*, 2015, **6**, 8249.
59 J.-W. Zhao, C.-F. Li, Z.-X. Shi, J.-L. Guan and G.-R. Li, *Research*, 2020, **2020**, 1–15.
60 A. Grimaud, O. Diaz-Morales, B. Han, W. T. Hong, Y. L. Lee, L. Giordano, K. A. Stoerzinger, M. T. M. Koper and Y. Shao-Horn, *Nat. Chem.*, 2017, **9**, 457–465.
61 D. A. Agyeman, Y. Zheng, T. H. Lee, M. Park, W. Tamakloe, G. H. Lee, H. W. Jang, K. Cho and Y. M. Kang, *ACS Catal.*, 2021, **11**, 424–434.
62 J. S. Yoo, X. Rong, Y. Liu and A. M. Kolpak, *ACS Catal.*, 2018, **8**, 4628–4636.
63 Y. Pan, X. Xu, Y. Zhong, L. Ge, Y. Chen, J. P. M. Veder, D. Guan, R. O'Hayre, M. Li, G. Wang, H. Wang, W. Zhou and Z. Shao, *Nat. Commun.*, 2020, **11**, 2002.
64 C. Yang and A. Grimaud, *Catalysts*, 2017, **7**, 149.
65 X. Rong, J. Parolin and A. M. Kolpak, *ACS Catal.*, 2016, **6**, 1153–1158.
66 Y. Zhou, Q. Gu, Y. Li, L. Tao, H. Tan, K. Yin, J. Zhou and S. Guo, *Nano Lett.*, 2021, **21**, 4861–4867.
67 D. Du, R. Zheng, M. He, C. Zhao, B. Zhou, R. Li, H. Xu, X. Wen, T. Zeng and C. Shu, *Energy Storage Mater.*, 2021, **43**, 293–304.
68 R. Li, J. Long, M. Li, D. Du, L. Ren, B. Zhou, C. Zhao, H. Xu, X. Wen, T. Zeng and C. Shu, *Mater. Today Chem.*, 2022, **24**, 100889.
69 H. Hou, Y. Cong, Q. Zhu, Z. Geng, X. Wang, Z. Shao, X. Wu, K. Huang and S. Feng, *Chem. Eng. J.*, 2022, **448**, 137684.
70 J. Zhang, C. Zhang, W. Li, Q. Guo, H. Gao, Y. You, Y. Li, Z. Cui, K. C. Jiang, H. Long, D. Zhang and S. Xin, *ACS Appl. Mater. Interfaces*, 2018, **10**, 5543–5550.
71 H. Gong, T. Wang, H. Guo, X. Fan, X. Liu, L. Song, W. Xia, B. Gao, X. Huang and J. He, *J. Mater. Chem. A*, 2018, **6**, 16943–16949.
72 Z. Wang, L. Zou, S. Guo, M. Sun, Y. Chen, B. Chi, J. Pu and J. Li, *J. Power Sources*, 2020, **468**, 228362.
73 X. Zhang, Y. Gong, S. Li and C. Sun, *ACS Catal.*, 2017, **7**, 7737–7747.
74 T. V. Pham, H. P. Guo, W. Bin Luo, S. L. Chou, J. Z. Wang and H. K. Liu, *J. Mater. Chem. A*, 2017, **5**, 5283–5289.
75 X. Li, Z. Qian, G. Han, B. Sun, P. Zuo, C. Du, Y. Ma, H. Huo, S. Lou and G. Yin, *ACS Appl. Mater. Interfaces*, 2020, **12**, 10452–10460.
76 R. Gao, Q. Chen, W. Zhang, D. Zhou, D. Ning, G. Schumacher, D. Smirnov, L. Sun and X. Liu, *J. Catal.*, 2020, **384**, 199–207.
77 R. S. Kalubarme, G.-E. Park, K.-N. Jung, K.-H. Shin, W.-H. Ryu and C.-J. Park, *J. Electrochem. Soc.*, 2014, **161**, A880–A889.
78 Z. Zhang, K. Tan, Y. Gong, H. Wang, R. Wang, L. Zhao and B. He, *J. Power Sources*, 2019, **437**, 226908.
79 C. Gong, L. Zhao, S. Li, H. Wang, Y. Gong, R. Wang and B. He, *Electrochim. Acta*, 2018, **281**, 338–347.
80 M. Y. Oh, J. H. Kim, Y. W. Lee, K. J. Kim, H. R. Shin, H. Park, K. T. Lee, K. Kang and T. H. Shin, *ACS Appl. Energy Mater.*, 2019, **2**, 8633–8640.
81 Y. Cong, Z. Geng, Q. Zhu, H. Hou, X. Wu, X. Wang, K. Huang and S. Feng, *Angew. Chem., Int. Ed.*, 2021, **60**, 23380–23387.
82 J. J. Xu, D. Xu, Z. L. Wang, H. G. Wang, L. L. Zhang and X. B. Zhang, *Angew. Chem., Int. Ed.*, 2013, **52**, 3887–3890.
83 H. Kim, Y. S. Lim and J. H. Kim, *Chem. Eng. J.*, 2022, **431**, 134278.
84 Q. Qiu, Z. Pan, P. Yao, J. Yuan, C. Xia and Y. Zhao, *Chem. Eng. J.*, 2023, **452**, 139608.
85 J. J. Xu, Z. L. Wang, D. Xu, F. Z. Meng and X. B. Zhang, *Energy Environ. Sci.*, 2014, **7**, 2213–2219.
86 P. Sennu, V. Aravindan, K. S. Nahm and Y. S. Lee, *J. Mater. Chem. A*, 2017, **5**, 18029–18037.
87 Z. Wang, X. Peng, S. Guo, M. Sun, J. Cheng, L. Zou, B. Chi and J. Pu, *ACS Appl. Energy Mater.*, 2021, **4**, 9376–9383.
88 S. Guo, L. Zou, M. Sun, Z. Wang, S. Han, B. Chi, J. Pu and J. Li, *ACS Appl. Energy Mater.*, 2020, **3**, 10015–10022.
89 J. G. Kim, Y. Kim, Y. Noh, S. Lee, Y. Kim and W. B. Kim, *ACS Appl. Mater. Interfaces*, 2018, **10**, 5429–5439.
90 Y. Cong, Z. Geng, Y. Sun, L. Yuan, X. Wang, X. Zhang, L. Wang, W. Zhang, K. Huang and S. Feng, *ACS Appl. Mater. Interfaces*, 2018, **10**, 25465–25472.
91 J. Jung, K. Song, Y. Bae, S. Il Choi, M. Park, E. Cho, K. Kang and Y. M. Kang, *Nano Energy*, 2015, **18**, 71–80.
92 G. Y. Qiao, D. Guan, S. Yuan, H. Rao, X. Chen, J. A. Wang, J. S. Qin, J. J. Xu and J. Yu, *J. Am. Chem. Soc.*, 2021, **143**, 14253–14260.
93 J. Kim, H. Kim, S. Shin, H. W. Lee and J. H. Kim, *Electrochim. Acta*, 2022, **412**, 140097.
94 Y. Bu, G. Nam, S. Kim, K. Choi, Q. Zhong, J. H. Lee, Y. Qin, J. Cho and G. Kim, *Small*, 2018, **14**, 1802767.
95 H. Lin, P. liu, S. Wang, Z. Zhang, Z. Dai, S. Tan and D. Chen, *J. Power Sources*, 2019, **412**, 701–709.
96 J. Zhang, Y. Zhao, X. Zhao, Z. Liu and W. Chen, *Sci. Rep.*, 2014, **4**, 2–7.
97 M. Sun, L. Zou, Z. Wang, S. Guo, Y. Chen, B. Chi, J. Pu and J. Li, *Electrochim. Acta*, 2019, **327**, 135017.
98 X. Li, T. Zhu, C. Wen, Y. Yang, S. Ma, X. Huang, H. Li and G. Sun, *Electrochim. Acta*, 2019, **317**, 367–374.
99 X. Han, Y. Hu, J. Yang, F. Cheng and J. Chen, *Chem. Commun.*, 2014, **50**, 1497–1499.

100 Y. Zhu, W. Zhou, J. Yu, Y. Chen, M. Liu and Z. Shao, *Chem. Mater.*, 2016, **28**, 1691–1697.
101 X. Xu, Y. Pan, L. Ge, Y. Chen, X. Mao, D. Guan, M. Li, Y. Zhong, Z. Hu, V. K. Peterson, M. Saunders, C. Te Chen, H. Zhang, R. Ran, A. Du, H. Wang, S. P. Jiang, W. Zhou and Z. Shao, *Small*, 2021, **17**, 2101573.
102 Y. Bu, O. Gwon, G. Nam, H. Jang, S. Kim, Q. Zhong, J. Cho and G. Kim, *ACS Nano*, 2017, **11**, 11594–11601.
103 V. Celorrio, L. Calvillo, G. Granozzi, A. E. Russell and D. J. Fermin, *Top. Catal.*, 2018, **61**, 154–161.
104 I. Yamada, H. Fujii, A. Takamatsu, H. Ikeno, K. Wada, H. Tsukasaki, S. Kawaguchi, S. Mori and S. Yagi, *Adv. Mater.*, 2017, **29**, 1603004.
105 U. A. Palikundwar, V. B. Sapre, S. V. Moharil and K. R. Priolkar, *J. Phys.: Condens. Matter*, 2009, **21**, 235405.
106 J. Cheng, Y. Jiang, M. Zhang, Y. Sun, L. Zou, B. Chi, J. Pu and L. Jian, *ChemCatChem*, 2018, **10**, 1635–1642.
107 Z. Du, P. Yang, L. Wang, Y. Lu, J. B. Goodenough, J. Zhang and D. Zhang, *J. Power Sources*, 2014, **265**, 91–96.
108 Y. Lv, Z. Li, Y. Yu, J. Yin, K. Song, B. Yang, L. Yuan and X. Hu, *J. Alloys Compd.*, 2019, **801**, 19–26.
109 S. Peng, X. Han, L. Li, S. Chou, D. Ji, H. Huang, Y. Du, J. Liu and S. Ramakrishna, *Adv. Energy Mater.*, 2018, **8**, 1800612.
110 J. Ran, T. Wang, J. Zhang, Y. Liu, C. Xu, S. Xi and D. Gao, *Chem. Mater.*, 2020, **32**, 3439–3446.
111 R. B. Wexler, G. S. Gautam, E. B. Stechel and E. A. Carter, *J. Am. Chem. Soc.*, 2021, **143**, 13212–13227.
112 S. Biniazi, H. Asgharzadeh, I. Ahadzadeh, O. Aydin and M. Farsak, *Dalton Trans.*, 2022, **51**, 18284–18295.
113 Y. Yang, W. Yin, S. Wu, X. Yang, W. Xia, Y. Shen, Y. Huang, A. Cao and Q. Yuan, *ACS Nano*, 2016, **10**, 1240–1248.
114 L. Zou, S. Guo, Z. Wang, M. Sun, F. Yu, B. Chi and J. Pu, *Electrochim. Acta*, 2021, **381**, 138219.
115 Y. Gong, X. Zhang, Z. Li, Z. Wang, C. Sun and L. Chen, *ChemNanoMat*, 2017, **3**, 485–490.
116 K. R. Yoon, D. S. Kim, W. H. Ryu, S. H. Song, D. Y. Youn, J. W. Jung, S. Jeon, Y. J. Park and I. D. Kim, *ChemSusChem*, 2016, **9**, 2080–2088.
117 Q. Cui, L. Ma, P. Zhang, Y. Cao and J. Wang, *J. Energy Chem.*, 2021, **57**, 401–405.
118 L. Zou, Z. Lu, Z. Wang, B. Chi and J. Pu, *J. Am. Ceram. Soc.*, 2022, **105**, 2690–2701.
119 M. Sun, S. Guo, Z. Wang, L. Zou, B. Chi, J. Pu and J. Li, *Electrochim. Acta*, 2020, **363**, 137235.
120 Y. Fang, Y. Fang, R. Zong, Z. Yu, Y. Tao and J. Shao, *J. Mater. Chem. A*, 2022, **10**, 1369–1379.
121 H. Li, Y. Chen, J. Z. Y. Seow, C. Liu, A. C. Fisher, J. W. Ager and Z. J. Xu, *Small Sci.*, 2022, **2**, 2100048.
122 B. Bao, Y. Liu, M. Sun, B. Huang, Y. Hu, P. Da, D. Ji, P. Xi and C. H. Yan, *Small*, 2022, **18**, 2201131.
123 C. E. Beall, E. Fabbri and T. J. Schmidt, *ACS Catal.*, 2021, **11**, 3094–3114.
124 A. Grimaud, A. Demortiere, M. Saubanere, W. Dachraoui, M. Duchamp, M. L. Doublet and J. M. Tarascon, *Nat. Energy*, 2017, **2**, 16189.
125 J. A. Esterhuizen, B. R. Goldsmith and S. Linic, *Nat. Catal.*, 2022, **5**, 175–184.
126 A. Chen, X. Zhang and Z. Zhou, *InfoMat*, 2020, **2**, 553–576.
127 X. Huang, Q. Guo, D. Yang, X. Xiao, X. Liu, Z. Xia, F. Fan, J. Qiu and G. Dong, *Nat. Photonics*, 2020, **14**, 82–88.
128 Q. Liang, Y. Zhao, J. De Chen, J. J. Dai, X. Ding, Z. Tong, S. J. Xie, J. Zhang, Z. H. Zhou, J. T. Li, J. F. Li and Y. Zhou, *Chem. Mater.*, 2022, **34**, 5607–5620.
129 B. J. Kim, D. H. Kim, S. L. Kwon, S. Y. Park, Z. Li, K. Zhu and H. S. Jung, *Nat. Commun.*, 2016, **7**, 11735.